CHANDRA
X-ray Center 60 Garden St., Cambridge Massachusetts 02138 USA

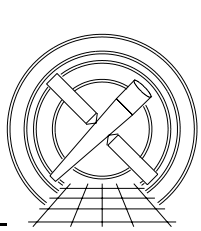

MEMORANDUM

Date: June 24, 2002
From: T. J. Gaetz
To: Distribution
Subject: Assessing the *Chandra* PSF Wings: An Estimate from Ground Calibration Data
File: `PSF_wing_profile_XRCF.tex`
Version: `1.0`

---

1 Summary

In this memo, the ground calibration data for the wings of the *Chandra* point spread function are considered. Coefficients for fits to "$2W_1(f)$" for the four individual mirror pairs are presented in Table 1, and these fits are compared to the ground data in Appendix B. There is considerable spread between the measurements (several $\times 0.1$ dex); the percentiles encompassing the central 68.3% of the points are plotted in Appendix C. The $2W_1(f)$ fits for individual shells are evaluated as surface brightness profiles, and compared to the measured profiles in Appendix D.

Finally, a prescription for combining the individual shell $2W_1(f)$ fits into surface brightness profiles for the full HRMA is given in Eq. 26. Because the $2W_1(f)$ are a measure of the surface roughness properties of the mirrors, the functions may be scaled to allow evaluation of the wing surface brightness profiles at different energies. The full HRMA surface brightness profiles are evaluated for several energies and presented in Fig. 1. The integrated surface brightness outside a radius θ (an "excluded energy", the fraction of the PSF outside θ) was computed from the above profiles and is presented in Fig. 2.

The data are also presented as ASCII (RDB and HTML) tables:

There remain systematics and uncertainties which need to be explored. In particular, the experimental configuration resulted in a nonuniform illumination of the HRMA and the roughest parts of the mirrors (the regions near the edges) are under-illuminated; consequently, the profiles are likely lower limits, particularly at large angles. The effect of the tilting of the HRMA in the ground test may also introduce a bias. These will be evaluated

by comparing with on-orbit data, which are subject to different systematics. In particular, any source extent or scattering by intervening dust will tend to result in an overestimate of the true PSF wings.

2 Evaluation of the *Chandra* PSF Wings: An Estimate from Ground Calibration Data

The *Chandra* High Resolution Mirror (HRMA) consists of 4 nested Wolter type I grazing incidence optics, each consisting of a paraboloidal mirror (P) and a hyperboloidal mirror (H). These are referred to as "mirror pairs" or "shells" interchangeably. For historical reasons, the shells are labeled 1, 3, 4, and 6 (from largest to smallest, respectively).

During the ground calibration at the X-ray Calibration Facility (XRCF), an extensive set of measurements was performed in order to validate the calibration raytrace model. The wing scan experiment was designed to map out the far wings of the Point Spread Function, or PSF, at angles $\gtrsim$1 mm (about $20''$ away from the core). Because of time constraints, only a selected portions of the wings could be mapped in detail. This was accomplished by a series of horizontal (Y) or vertical (Z) pinhole scans through the PSF, using pinholes with nominal diameters of 1, 4, 10, 20, and 35 mm. Each scan was centered on the core of the PSF, and up to 3 points were sampled to either side (*i.e.*, $-3D_{ap}$, $-2D_{ap}$, $-1D_{ap}$, 0, $+1D_{ap}$, $+2D_{ap}$, $+3D_{ap}$).

Quadrant shutters were used to isolate quadrants of individual mirror pairs (or *shells*) of the optic. Wing scans were performed at various energies for various quadrants of individual mirror pairs. The combinations of quadrant, energy, and pinhole diameter for the single quadrant wing scans are given in Table 2.

The far wings of the PSF result mainly from scattering by the optic surfaces, primarily scattering from microroughness. In principle dust scattering could also contribute, but any dust component was expected to be small because of the cleanliness of the *Chandra* optics, and a special set of transverse wing scans at C-Kα (0.277 keV) confirmed that scattering from dust on the mirrors was not a significant component.

For grazing incidence reflection, scattering by microroughness is predominantly in-plane with only a small out-of-plane component. Consequently, Y-scans were performed for the North and South quadrants, while Z-scans were used for the Top and Bottom quadrants; a Y-scan was also performed at C-Kα for the shell 6 bottom quadrant in order to look for out-of-plane scattering resulting from any dust contamination. (In the following, I use the terms "mirror pair" and "shell" interchangeably.)

In the ground calibration measurements for individual mirror quadrants, the HRMA was

tilted in order to obtain a more nearly on-orbit incidence angle for the beam in order to obtain a better illumination of the optics. Because the X-ray sources were at finite distance, the beam diverged slightly; as a result, the effective illumination pattern on the projected surface of the P optic was not uniform (as would be expected for an ideal system with the source at infinite distance). In particular, this led to the ends of the optics (known from mirror metrology to be rougher than the middles of the optics) being less well illuminated.

The intent of the ground calibration was to verify and validate a detailed raytrace model for the optics by using detectors with absolute calibrations. The raytrace model includes various ground testing effects, such as the finite distance to the source, and detailed finite-element mechanical models of the geometrical deformation of the optics under gravity as supported by the mirror support structures. The baseline on-orbit calibration model could then be obtained by replacing the 1G finite element model with an appropriate on-orbit model (*i.e.*, turning off gravity in the model).

This approach has worked very well, particularly for reproducing the overall image aberrations induced by the misalignments within the optics. Modeling the scattering has proven more problematic, though. The scattering function is based on detailed metrology of the roughness of the optics, with 5 to 11 axial zones per optic representing the variation in surface roughness along the optic. The middle of the optic (typically $\sim 80\%$) is smoothest, with increasing roughness toward the edges. Mirror pair 1, the largest mirrors, also have the roughest surfaces. The scattering model is based on Kirchoff scalar diffraction theory. Unfortunately, the model tends to underpredict the wings of the PSF; refinements of the model and scattering function for the wings are under investigation. In this memo, I develop an in interim model for the HRMA wings profile based directly on the ground calibration data.

3 General Considerations

Because of the differences between ground and on-orbit configurations, a number of systematic effects come in. In particular:

- Time limitations led to a sparse sampling for energies and mirror quadrants (see Appendix A). Note that for energies higher than 4.51 keV, some mirror pairs were not measured at all. This is particularly a problem at 5.41 keV; the large outermost mirror pair still has significant on-axis effective area ($\sim$ 13% of the total); by 6.4 keV, the mirror pair 1 contribution drops to $\sim$ 1.4%. Although the shell 1 effective area at high energies is small compared to the inner shells, mirror pair 1 also has the roughest surface.
- Absolute scaling of the wings: The pinhole effective areas were normalized with ab-

solutely calibrated detectors. However deriving the wing normalization is subject to systematic effects:

  - A quadrant shutter scaling factor needs to be applied. Scattering from microroughness is mainly in-plane, so the quadrant shutters block $\sim 1/2$ of scattered the scattered flux for off-axis pinholes, but only $\sim 1/4$ ($\sim 88/360$, taking into account shutter blade overlap) of the specular flux in the on-axis pinhole central pinhole position (*i.e.*, the pinhole containing the direct specular image of the source). This correction factor is thus approximately 2, but it should be modeled. For now, the quadrant shutter correction factor is taken to be exactly 2.
  - The optics were tilted to obtain a mean graze angle more nearly corresponding to the on-orbit graze angle for the given mirror pair. This improves the illumination pattern, but does not completely replicate the on-orbit conditions. The illumination pattern varies azimuthally around the quadrant, and the graze angle varies axially along the optic; these systematically affect the fluxes. Again, this correction should be modeled.

- The tilt of the optics (in order to improve the illumination pattern) results in the rough ends of the optics being undersampled relative to the smoother interior of the optic. It would thus be expected that the straightforward combination of the wing scan measurements will systematically underestimate the slope of the wings.
- The closed shutters (required to isolate particular mirror quadrants) result in significant vignetting by the quadrant shutter blades for far off-axis angles. This is particularly important for the middle two mirror pairs (3 and 4) because of their close spacing.

These considerations should be kept in mind.

In the following, the wings are analyzed separately for each mirror pair. All the pinhole scan data are combined for each mirror pair and energy; pinholes are not included if they are geometrically vignetted by the quadrant shutters. The resulting single-mirror-pair wings are normalized using an on-axis measurement of effective area within the 35 mm diameter pinhole (or interpolated if a direct measurement is not available).

3.1 Analysis Strategy

For shell s, pinhole p:

$\mathcal{R}_p^{(s)}(\theta)$	= count rate, pinhole p, (cts s^{-1})
$\mathcal{R}_{35mm}^{(s)}(0)$	= count rate, on-axis 35mm pinhole, full shell, (cts s^{-1})
$\Omega_p^{(s)}$	$= \pi \left(d_p^{(s)}/4F_{fc} \right)^2$ = solid angle, pinhole p, (sterad)
$w_p^{(s)}$	= pinhole correction factor (slope of wing profile across pinhole)
$f_{qc}^{(s)}$	~ 2, quadrant shutter correction factor; scattering is mainly in-plane: off-axis pinhole gets $\sim 1/2$ of scattered flux; on-axis pinhole gets $\sim 1/4$ specular flux.

Procedure:

- Remove pinholes geometrically vignetted by quadrant shutters.
- Evaluate the surface brightness corresponding to each pinhole off-axis position, for each shell and energy, based on the measured pinhole A_{eff}. This surface brightness is normalized to the full shell on-axis 35 mm diameter pinhole effective area, $A_{eff,35}$.
- From the surface brightness, evaluate $2W_1^{(s)}(f)$ for each shell (Eq. 16).
- For each shell, fit an exponentially truncated (possibly broken) powerlaw to the the $2W_1^{(s)}(f)$.
- From the $2W_1$ fits for the individual shells, for a given energy, evaluate the surface brightness as a function of off-axis angle (Eq. 24).
- Combine the per-shell surface brightnesses to form the total HRMA surface brightness (Eq. 25).

4 Analysis

Let

$$\mathcal{R}_p^{(s)} = \text{count rate, shell s, pinhole p, (cts s}^{-1}) \quad (1)$$

$$\mathcal{R}_{BND} = \text{count rate, BND, (cts s}^{-1}) \quad (2)$$

$$A_{BND} = \text{open area, BND, (cm}^2) \quad (3)$$

where the subscript *BND* refers to the Beam Normalization Detectors (BND). The effective area for pinhole p is evaluated as

$$A_{eff,p}^{(s)} = A_{BND} \frac{\mathcal{R}_p^{(s)}}{\mathcal{R}_{BND}} \text{ cm}^2 \quad (4)$$

The area of the pinhole is

$$A_{p,mm} = \frac{\pi d_p^2}{4} \text{ mm}^2 \tag{5}$$

where d_p is the diameter of the pinhole in mm.

The solid angle subtended by the pinhole is

$$\Omega_p = \frac{A_p}{F_{fc}^2} \text{ sterad} \tag{6}$$

$$= \pi \left[\frac{4.8481368 \times 10^{-6} d_p}{2F_{fc}} \right]^2 \text{ arcsec}^2 \tag{7}$$

where F_{fc} is the finite conjugate focal length (nominally 10275 mm) appropriate to the XRCF ground calibration configuration.

For each pinhole size and position, we define a pinhole correction factor, w, as

$$w \approx \frac{1}{{}_2F_1\left(\frac{\gamma}{2}, \frac{\gamma}{2}, 2; \frac{a^2}{r_p^2}\right)} \tag{8}$$

where a is the pinhole radius, r is the off-axis distance, and ${}_2F_1$ is a hypergeometric function. This factor accounts for the slope of the PSF across the pinhole; this is particularly important for the nearest off-axis points in each scan, which are offset by only a pinhole diameter from the specular image. The value of γ was obtained by using the local logarithmic derivative of the fit function location of the pinhole center.

Thus, the surface brightness at the location of the pinhole is estimated as

$$\mathcal{S}_p^{(s)} = \frac{\mathcal{R}_p^{(s)}}{\Omega_p} (\text{cts s}^{-1} \text{ sterad}^{-1}) \tag{9}$$

Let

$$\mathcal{F} = \frac{\mathcal{R}_{BND}}{A_{BND}} (\text{cts s}^{-1} \text{ cm}^{-2}) \tag{10}$$

be the source flux as seen by the BND's. The normalized surface brightness is then

$$\mathcal{S}_{norm,p}^{(s)} = \frac{\mathcal{S}_p^{(s)}}{\mathcal{F}} \tag{11}$$

$$= \frac{\mathcal{R}_p^{(s)}}{\Omega_p^{(s)}} \frac{A_{BND}^{(s)}}{\mathcal{R}_{BND}^{(s)}} \tag{12}$$

$$= \frac{A_{eff,p}^{(s)}}{\Omega_p^{(s)}} (\text{ cm}^2 \text{ sterad}^{-1}) \tag{13}$$

Finally, apply the pinhole correction factor and normalize by the total 35 mm pinhole effective area for the shell

$$\mathcal{S}^{(s),corr}_{norm,p} = w^{(s)}_p \frac{\mathcal{S}^{(s)}_{norm,p}}{A^{(s)}_{eff,35}} \tag{14}$$

This represents the estimate for the normalized surface brightness, (cts s^{-1} $arcsec^{-2}$ / source cts s^{-1}).

4.1 Surface Brightness and $2W_1$

For a given mirror pair, the surface brightness profiles at different energies can be combined to estimate PSD "$2W_1$" functions describing the surface roughness. Each spatial frequency in the roughness distribution diffracts the X-rays according to the diffraction equation. For grazing incidence reflection at graze angle α, and X-ray wavelength λ, the first order diffraction angle θ is related to the spatial frequency f by

$$f = \theta \sin\alpha/\lambda \tag{15}$$

The value of $2W_1$ describing the one-dimensional PSD is (O'Dell *et al.* 1992, Eq. 7):

$$2W_1^{(s)}(f) = \frac{f\psi_E^{(s)}(\theta)}{16\pi}\left[\frac{\lambda}{\sin\alpha_{sh}}\right]^4\Big|_{f=\frac{\theta\sin\alpha_{sh}}{\lambda}} \tag{16}$$

or

$$2W_1^{(s)}(f) = \frac{\theta\psi_E^{(s)}(\theta)}{16\pi}\left[\frac{\lambda}{\sin\alpha_{sh}}\right]^3 \tag{17}$$

where $f = \theta\sin\alpha/\lambda$ is the spatial frequency corresponding to an X-ray with wavelength λ, θ is the off-axis angle, α is the mean graze angle for the mirror shell, λ is the X-ray wavelength, and $\psi_E^{(s)}$ is the surface brightness for shell sh at energy E, normalized to the on-axis effective area for the full shell, measured using the 35 mm diameter pinhole (*i.e.*, $\psi_E^{(s)} = \mathcal{S}^{corr}_{norm,p}$). Note that this definition provides $2W_1$ *per surface*; for the Wolter type I optic with two surfaces, X-ray scattering is double that implied by the $2W_1$ PSD. Conventionally, the $2W_1$ has units if $Å^2$mm, and the spatial frequency f has units mm^{-1}.

$2W_1$can be rewritten in terms of energy:

$$2W_1^{(s)}(f)\Big|_{f=\frac{\theta E\sin\alpha_{sh}}{hc}} = \frac{\theta\psi_E^{(s)}(\theta)}{16\pi}\left[\frac{hc}{E\sin\alpha_{sh}}\right]^3 \tag{18}$$

where h is Planck's constant and c is the speed of light.

The resulting $2W_1^{(s)}(f)$ values for each shell, sh, are fit to an exponentially truncated power law:

$$2W_1^{(s)}(f) = K_{b,sh} f^{-p_{1,sh}} \exp\left(-f/f_{0,sh}\right), \tag{19}$$

where $K_{b,sh}$ is the value of the fit at $f_{0,sh}$. The smaller mirror shells (MP4 and MP6) are steeper at smaller f, so these are fit to broken power laws with an exponential truncation:

$$\begin{aligned} 2W_1^{(s)}(f) &= K_{b,sh} f^{-p_{1,sh}} \exp\left(-f/f_{0,sh}\right), & f \le f_{b,sh} \quad (20) \\ &= K f_{b,sh}^{p_{2,sh}-p_{1,sh}} f^{-p_{2,sh}} \exp\left(-f/f_{0,sh}\right), & f > f_{b,sh} \quad (21) \end{aligned}$$

For simplicity in combining the fits, all the fits are tabulated in the form of exponentially truncated broken powerlaws; in the cases where only a single powerlaw is used, $p_{2,sh}$ and f_b are set to provide an equivalent broken powerlaw, *i.e.*,

$$\begin{aligned} p_{2,sh} &\equiv p_{1,sh} \quad (22) \\ f_b &\equiv 10 \quad (23) \end{aligned}$$

Given the resulting $2W_1$ fits, the surface brightness profile for a given shell is derived for a given energy:

$$\psi_{E,sh}(\theta) = 16\pi \left[\frac{E \sin\alpha_{sh}}{hc}\right]^3 \frac{2W_{1,sh}(f)}{\theta}\Big|_{f=\frac{\theta E \sin\alpha_{sh}}{hc}} \quad (24)$$

These are combined into a normalized surface brightness profile for the full HRMA:

$$\psi_{E,HRMA}(\theta) = \frac{16\pi}{\theta} \sum_{sh} \left\{ \frac{A_{eff,sh}}{A_{eff,HRMA}} \left[\frac{E \sin\alpha_{sh}}{hc}\right]^3 2W_{1,sh}(f)\Big|_{f=\frac{\theta E \sin\alpha_{sh}}{hc}} \right\} \quad (25)$$

or,

$$\begin{aligned} \psi_{E,HRMA}(\theta) &= \frac{1.2786 \times 10^{-18}}{\theta_{\rm arcsec}} \\ &\quad \times \sum_{sh} \left\{ \frac{A_{eff,sh}}{A_{eff,HRMA}} \left[E_{\rm keV} \sin\alpha_{sh}\right]^3 2W_{1,sh}(f)\Big|_{f(\theta_{\rm arcsec}, E_{\rm keV}, \sin\alpha_{sh})} \right\} \\ &\quad \left(\frac{\rm cts\ s^{-1}\ arcsec^{-2}}{\rm source\ cts\ s^{-1}}\right) \quad (26) \end{aligned}$$

where

$$f = 3.91025\, \theta_{\rm arcsec} E_{\rm keV} \sin\alpha_{sh} \quad {\rm mm}^{-1}, \quad (27)$$

$\theta_{\rm arcsec}$ is the angle (in arcsec) between the scattered photon and the direct image, and E_{keV} is the photon energy in keV. The $A_{eff,sh}$ and $A_{eff,HRMA}$ are the on-axis effective areas (nominally the 35 mm diameter pinhole effective areas, or where necessary, the interpolated effective area).

The resulting fit coefficients are given in Table 1. The f_{min} and f_{max} columns give the approximate range over which ground measurements are available.

Plots comparing the fits to the data are provided in Appendix B. There is a considerable spread in the data points (several $\times 0.1$ dex); see the bottom panels in Appendix B.

To better quantify the the distribution, the data were binned in broad f ranges (< 2, 2–5, 5–10, 10–20, 20–50, 50–100, 100–200, and > 200). The 15.85% and 84.15% percentiles (enclosing the central 68.3% of the points) were computed for the distributions of $\log_{10} 2W_1(data)/2W_1(model)$. The results are plotted in Appendix C. There remain systematic trends in the fits *vs.* the data, so the fits should be regarded as provisional.

The surface brightness profiles for individual shells were evaluated using Eq. 24 are in Appendix D.

Finally, surface brightness profiles for the full HRMA, evaluated at selected energies, are plotted in Fig. 1.

Table 1: $2W_1$ fit coefficients for individual shells

Shell	$p_{1,s}$	$p_{2,s}$	$f_{b,s}$	$K_{b,s}$	f_0	$\sin\alpha_s$	f_{min}	f_{max}
1	0.951	0.951	10.0	5.2	303.4	1.4893E-2	1.50	370
3	1.242	1.242	10.0	3.5	443.7	1.1984E-2	1.20	633
4	1.962	1.138	3.8	11.2	177.2	1.0588E-2	1.10	470
6	2.306	0.861	4.5	22.8	78.8	7.8539E-3	0.16	520

The integrated surface brightness outside a radius θ (an "excluded energy", the fraction of the PSF outside θ) was computed from the above profiles and is presented in Fig. 2.

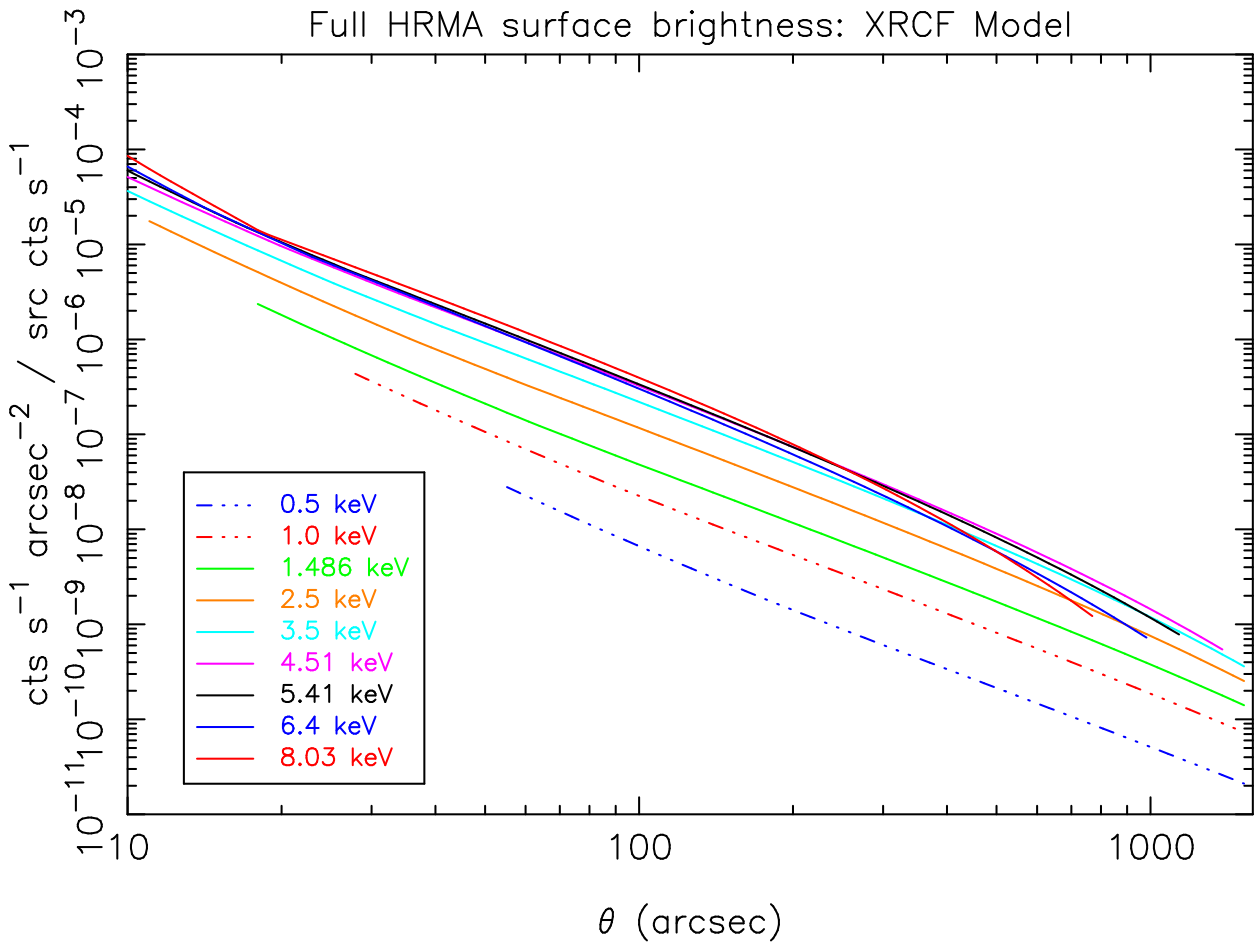

Figure 1: Surface brightness profile for the full HRMA, evaluated from the $2W_1$ fits to individual mirror pairs.

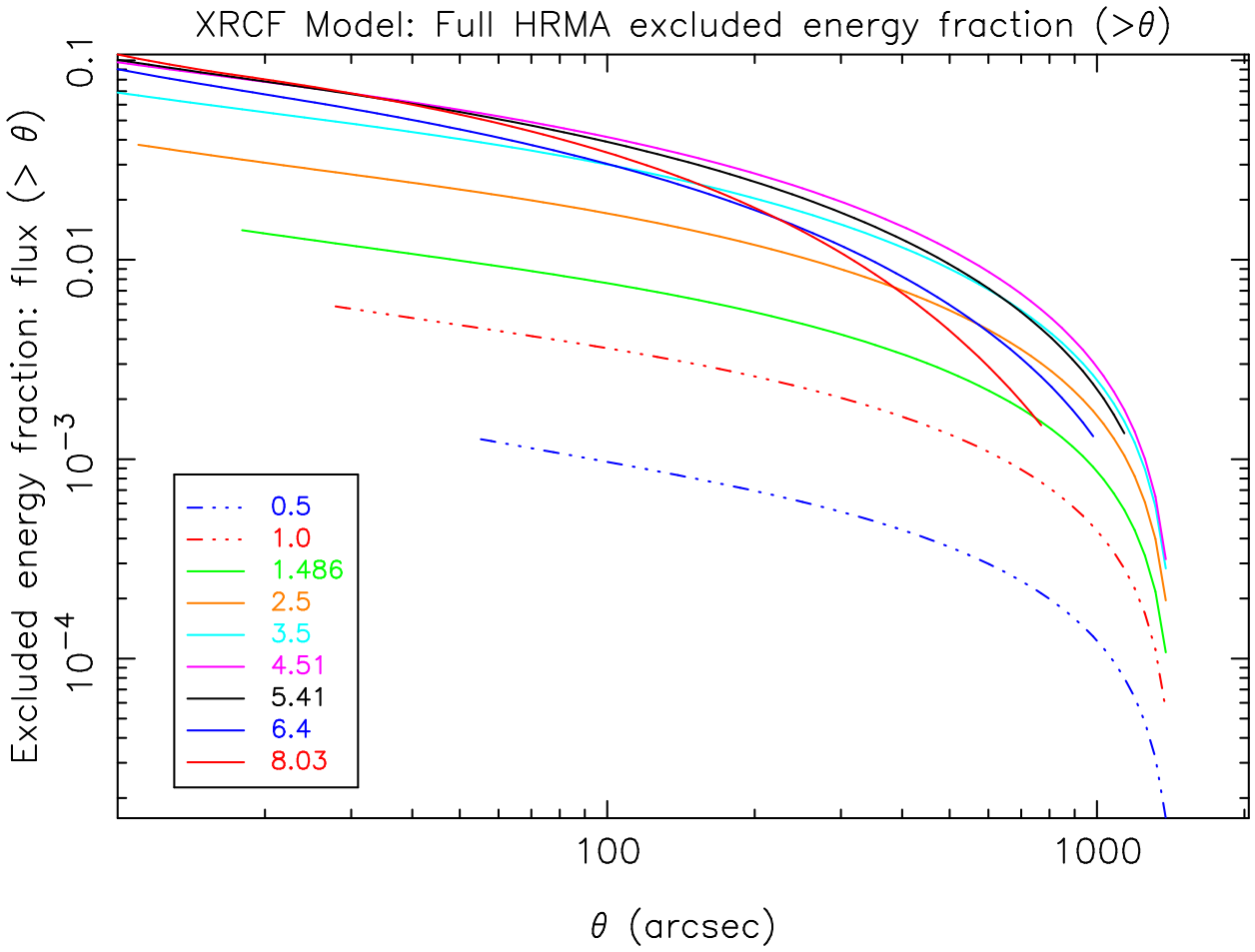

Figure 2: Flux fraction outside θ (excluded energy fraction). This is the integral of the profile outward from θ, based on the surface brightness profiles evaluated from the $2W_1$ fits to individual mirror pairs.

5 Caveats

This report discusses work in progress; the reduction and analysis will be revisited and redone as more is learned from analysis of other bright X-ray sources, and also as the understanding of the systematics in the ground calibration improves.

6 Suggestions for Future Work

- The $2W_1$ scaling allows the surface brightness profiles to be evaluated for different energies. For comparison with on-orbit data, the profile for a given energy band should be integrated over the source spectrum. This would take into account the variation of the profile with energy.
- The profiles can be improved using high quality on-orbit data for source with low N_H columns. Using the $2W_1$-based profiles as a baseline, the residuals can be parameterized as functions of energy and off-axis angle. The $2W_1$-based profiles can account for much of the energy and angular variation, with an empirical correction factor (probably energy dependent) accounting for the residuals.

A Wing Scan Measurements

Table 2: XRCF Single Quadrant Wing Scan Measurements (by shell and quadrant)

Energy (keV)	diam (mm)	T1	N1	B1	S1	T3	N3	B3	S3	T4	N4	B4	S4	T6	N6	B6	S6
0.277	1															•	
0.277	4															•	
0.277	10															•	
0.277	20															•	
0.277	35																
1.486	1	•	•	•	•	•	•	•	•	•	•	•	•	•	•	•	•
1.486	4	•	•	•	•	•	•	•	•	•	•	•	•	•	•	•	•
1.486	10	•	•	•	•		•		•		•		•		•		•
1.486	20	•	•	•	•	•	•	•	•	•	•	•	•	•	•	•	•
1.486	35		•		•		•		•		•		•		•		•
4.51	1	•	•	•	•				•				•				•
4.51	4	•	•	•	•				•				•				•
4.51	10	•	•	•	•				•				•				•
4.51	20	•	•	•	•				•				•				•
4.51	35		•		•				•				•				•
5.41	1								•				•				•
5.41	4								•				•				•
5.41	10								•				•				•
5.41	20								•				•				•
5.41	35								•				•				•
6.4	1					•	•	•	•	•	•	•	•	•	•	•	•
6.4	4					•	•	•	•	•	•	•	•	•	•	•	•
6.4	10					•	•	•	•	•	•	•	•	•	•	•	•
6.4	20					•	•	•	•	•	•	•	•	•	•	•	•
6.4	35						•				•		•		•		•
8.03	1												•	•	•†	•	•
8.03	4												•	•	•†	•	•
8.03	10												•	•	•†	•	•
8.03	20												•	•	•†	•	•
8.03	35												•		•†		•

†CMDB indicates yaw = $-1.88'$; other logs indicate that yaw = $+1.88'$ was actually used.

B $2W_1$ Fits for Individual Shells

In this appendix, the data for individual shells and energies are compared to the predictions based on the fits of $2W_1$ to the full data set for each shell.

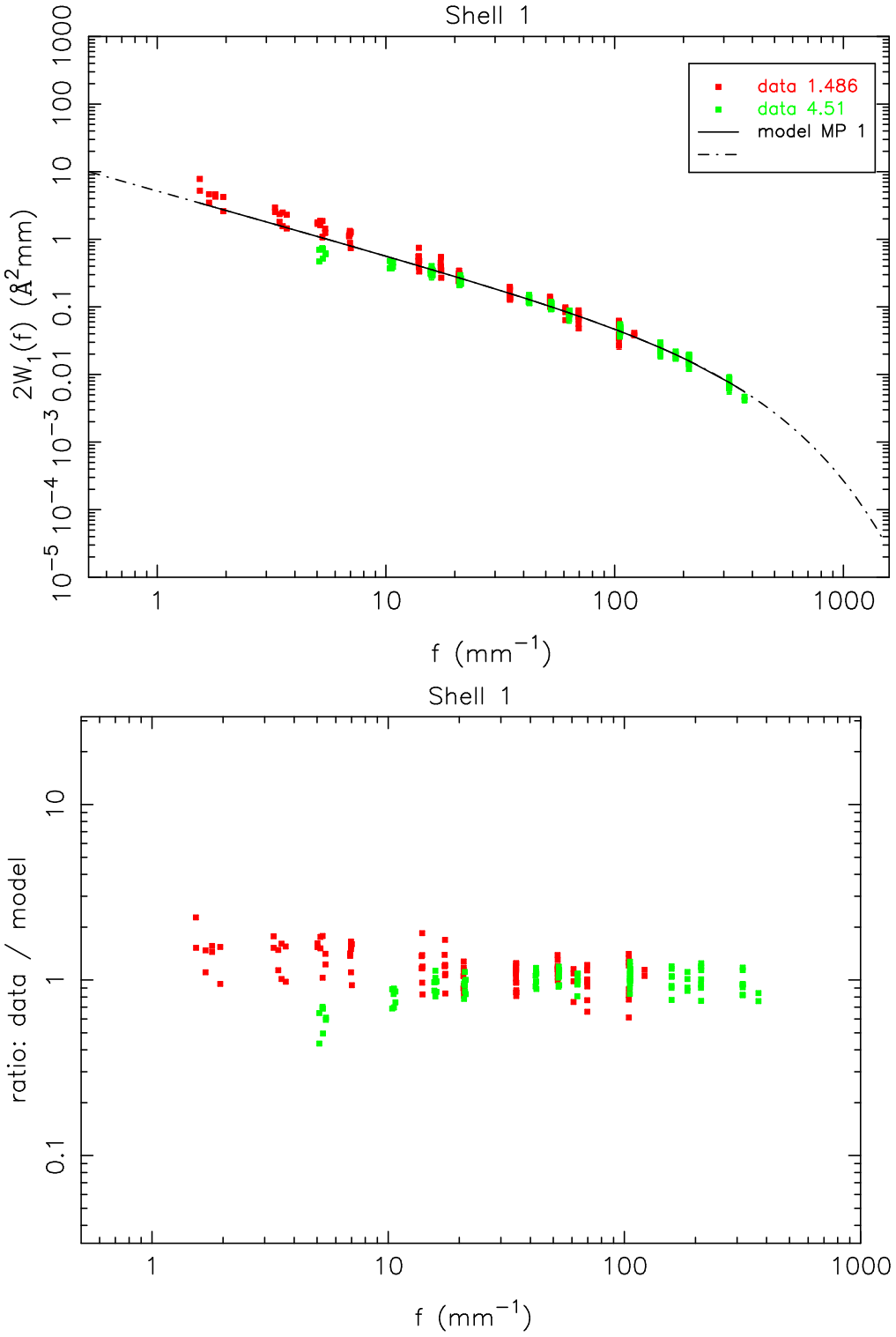

Figure 3: Top: Data and fit for shell 1. Bottom: Data/Model.

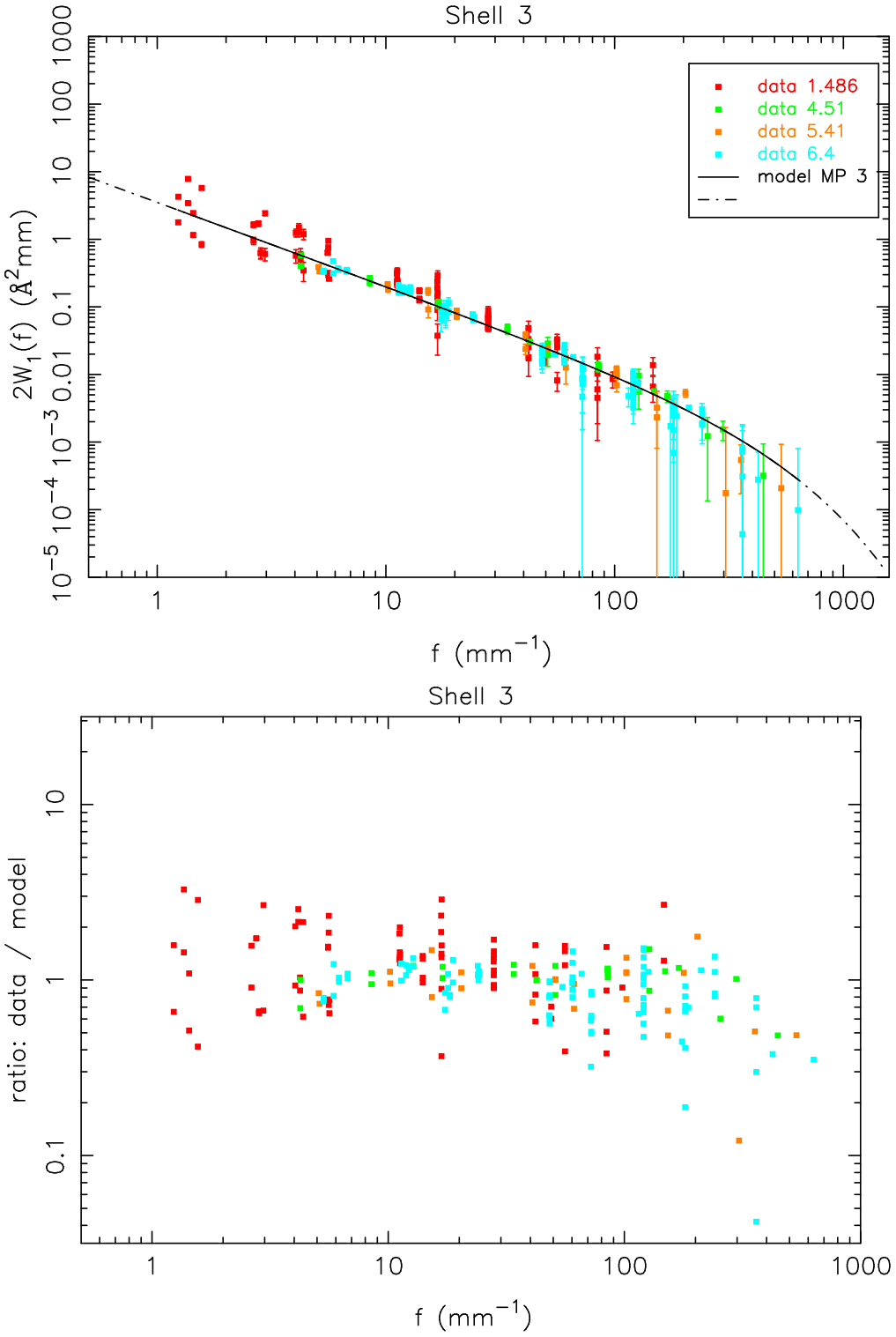

Figure 4: Top: Data and fit for shell 3. Bottom: Data/Model.

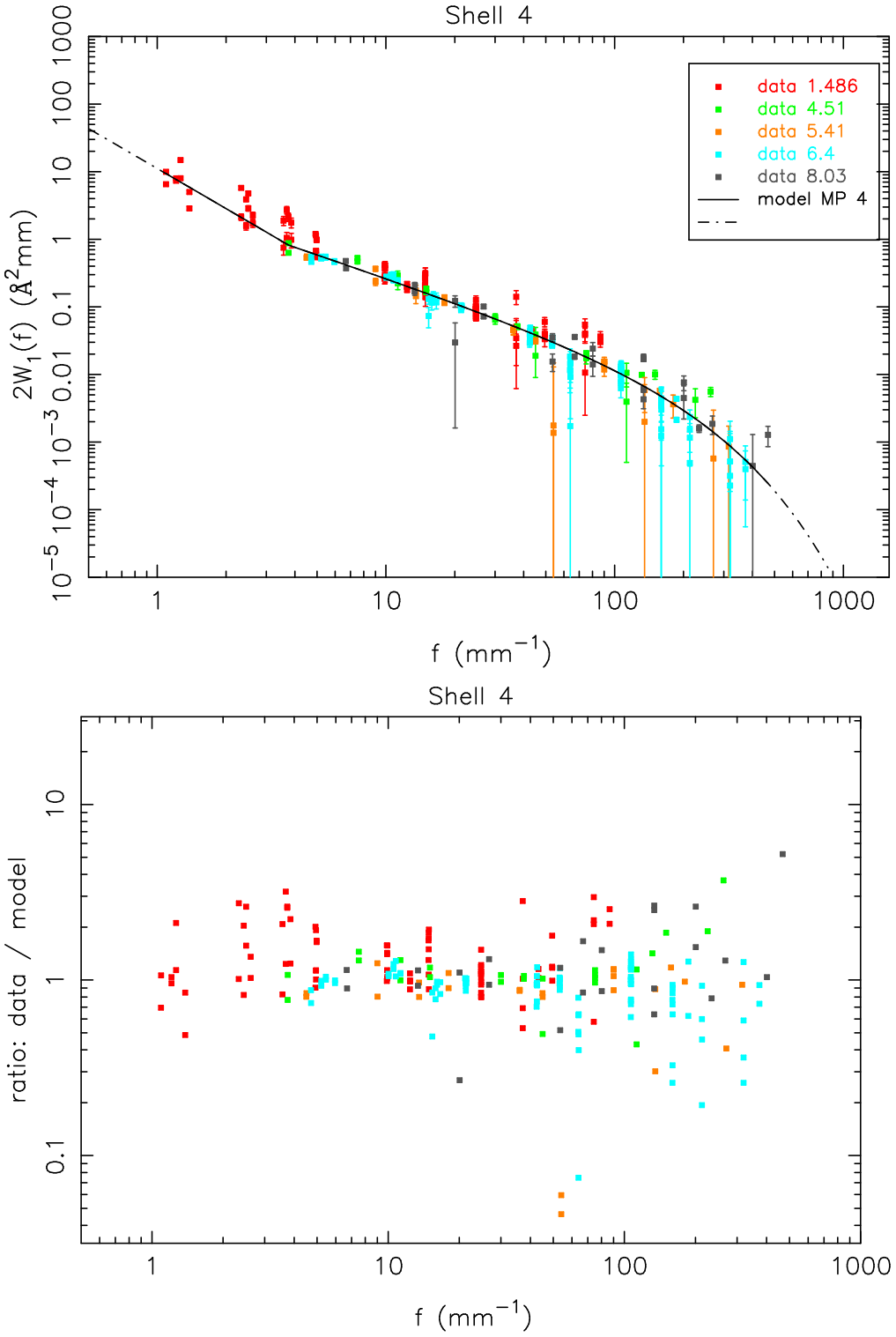

Figure 5: Top: Data and fit for shell 4. Bottom: Data/Model.

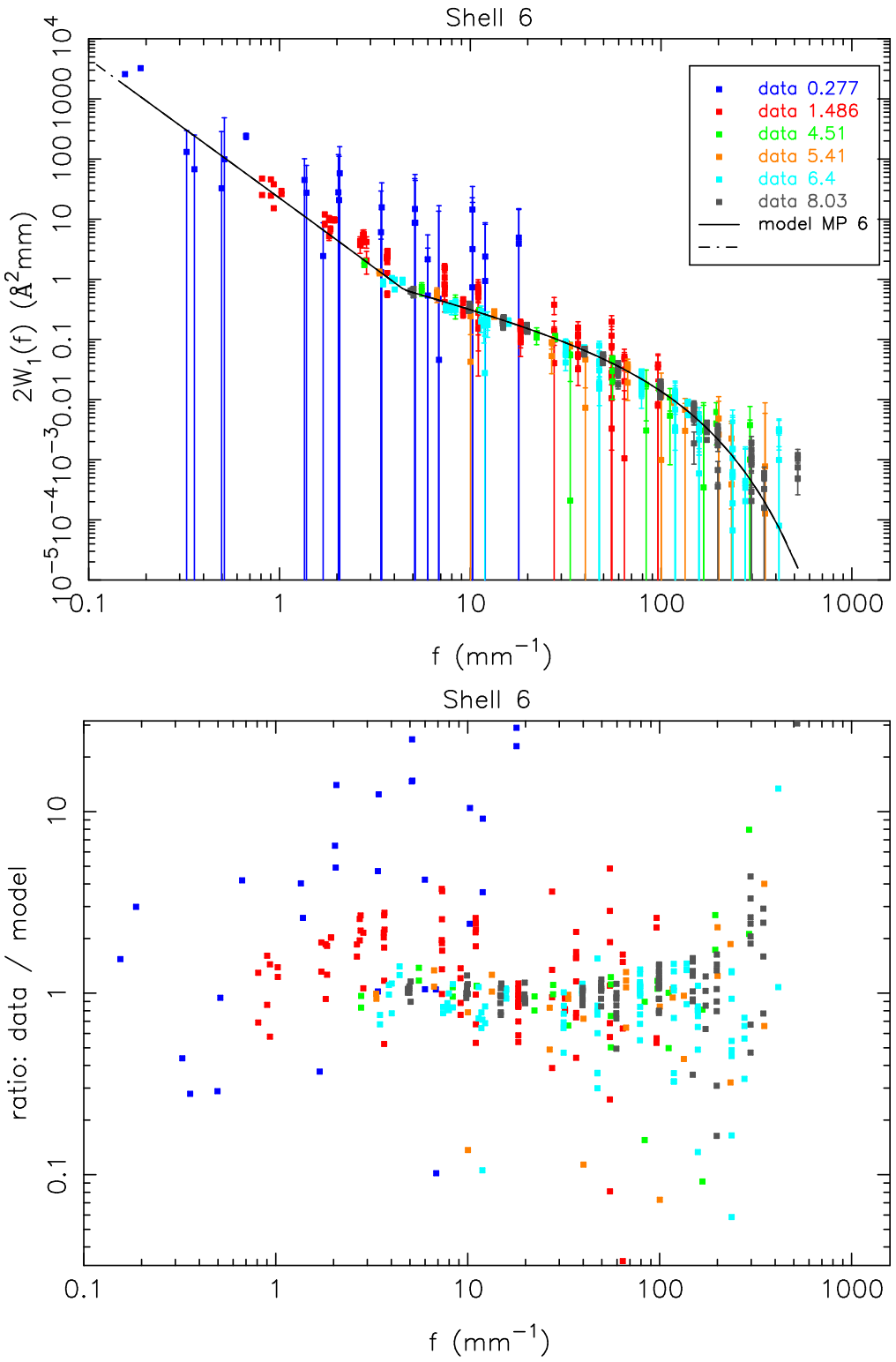

Figure 6: Top: Data and fit for shell 6. Bottom: Data/Model.

C Percentiles: $\log_{10} 2W_1(data)/2W_1(model)$ for Individual Shells

There is a considerable spread (several dex) in the data points; see the bottom panels in Appendix B. To better quantify the the distribution, the data were binned in broad f ranges (> 2, 2–5, 5–10, 10–20, 20–50, 50–100, 100–200, and > 200). The 15.85% and 84.15% percentiles (enclosing the central 68.3% of the points) were computed for the distributions of $\log_{10} 2W_1(data)/2W_1(model)$. In these figures, the points indicate the median values for $\log_{10} 2W_1(data)/2W_1(model)$. The lower error bar indicates the 15.85% percentile and the upper error bar the 84.15% percentile. That is, the error bars enclose the central 68.3% of the distribution. The horizontal error bars indicate the range in the f values within each broad bin.

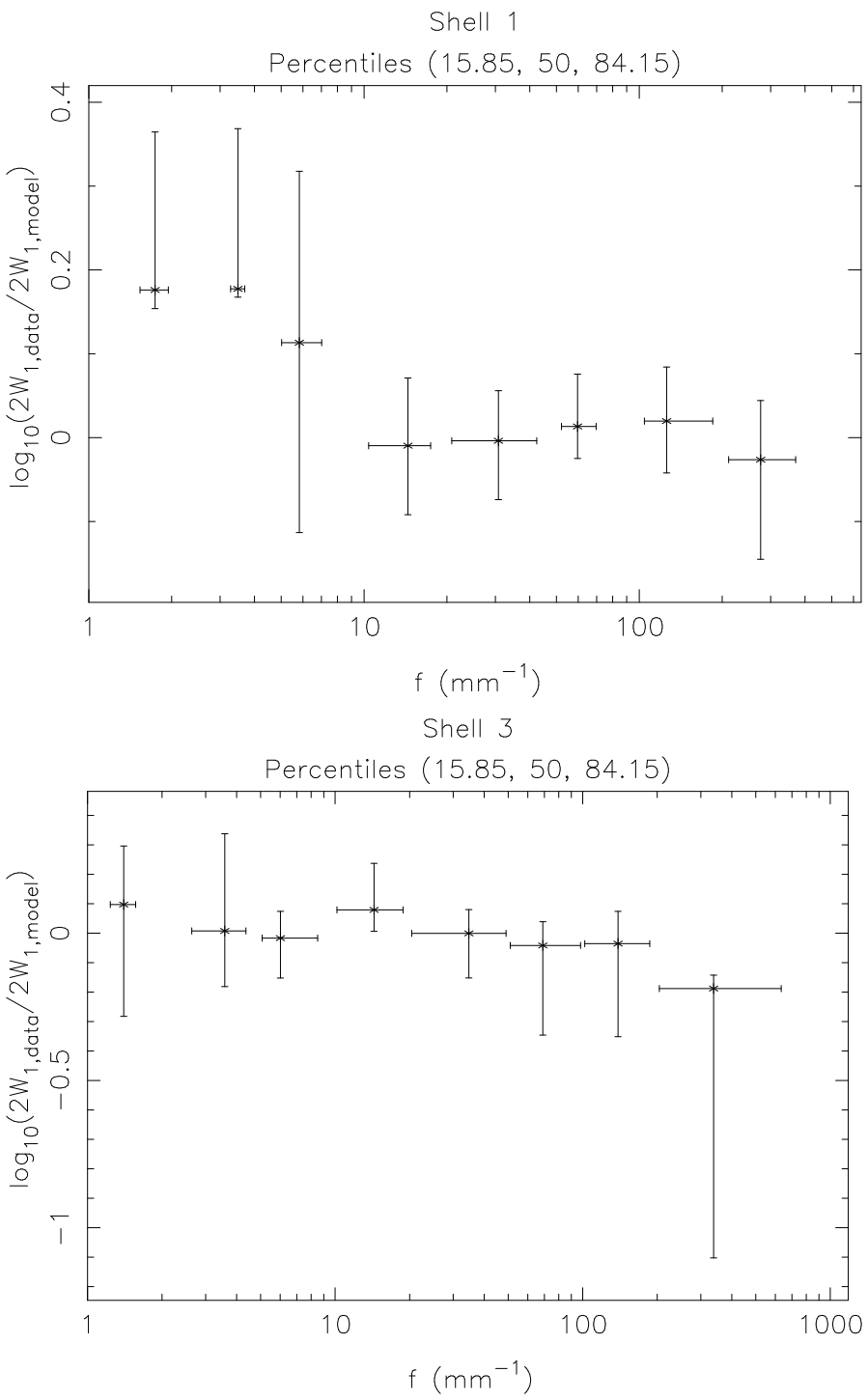

Figure 7: Top: 15.85%, 50%, and 84.15% percentiles of $\log_{10} 2W_1(data)/2W_1(model)$ for shell 1. The horizontal error bar indicates the range of f values in the bin. Bottom: 15.85%, 50%, and 84.15% percentiles of $\log_{10} 2W_1(data)/2W_1(model)$ for shell 3. The horizontal error bar indicates the range of f values in the bin.

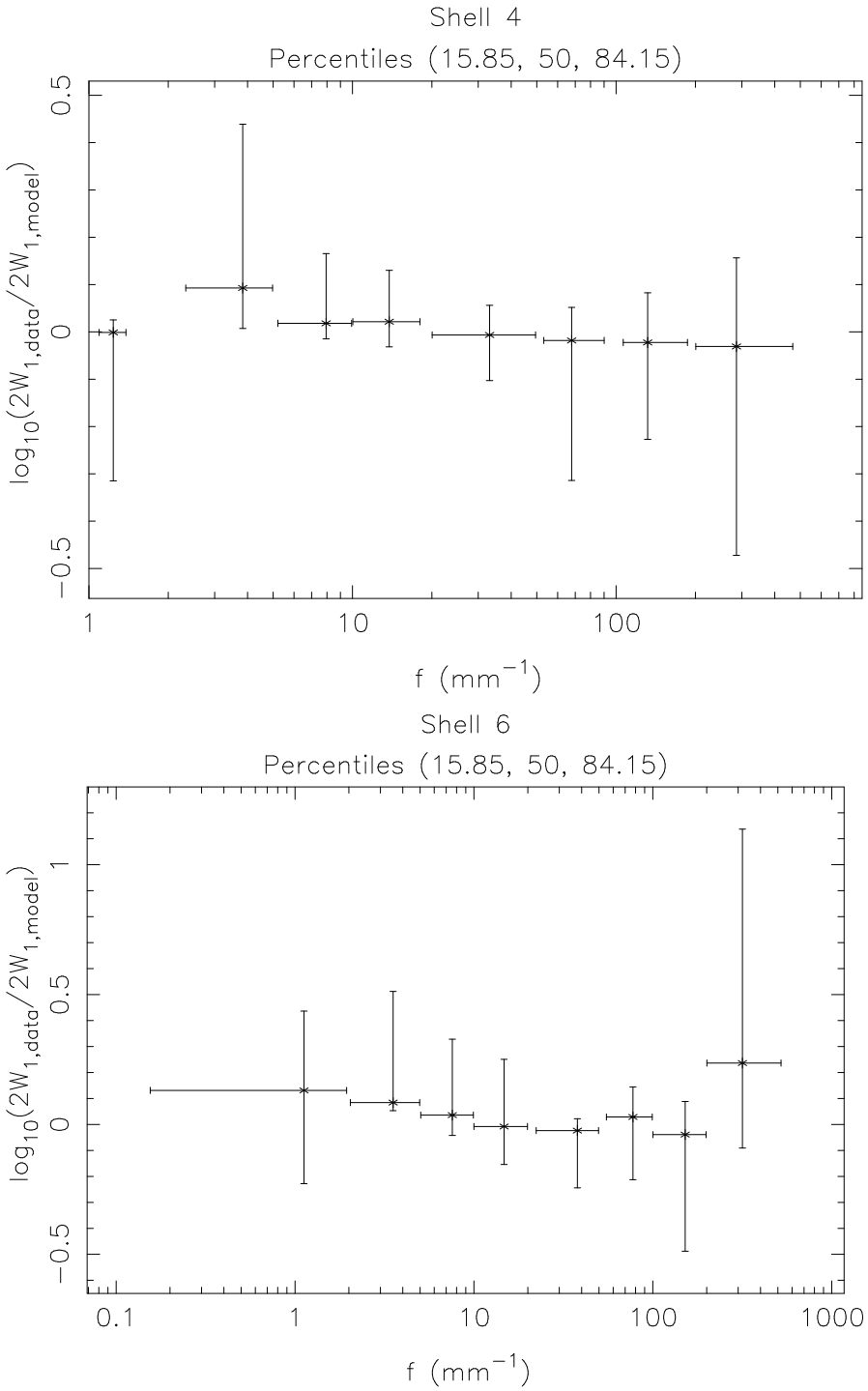

Figure 8: Top: 15.85%, 50%, and 84.15% percentiles of $\log_{10} 2W_1(data)/2W_1(model)$ for shell 4. The horizontal error bar indicates the range of f values in the bin. Bottom: 15.85%, 50%, and 84.15% percentiles of $\log_{10} 2W_1(data)/2W_1(model)$ for shell 6. The horizontal error bar indicates the range of f values in the bin.

D Surface Brightness Profiles

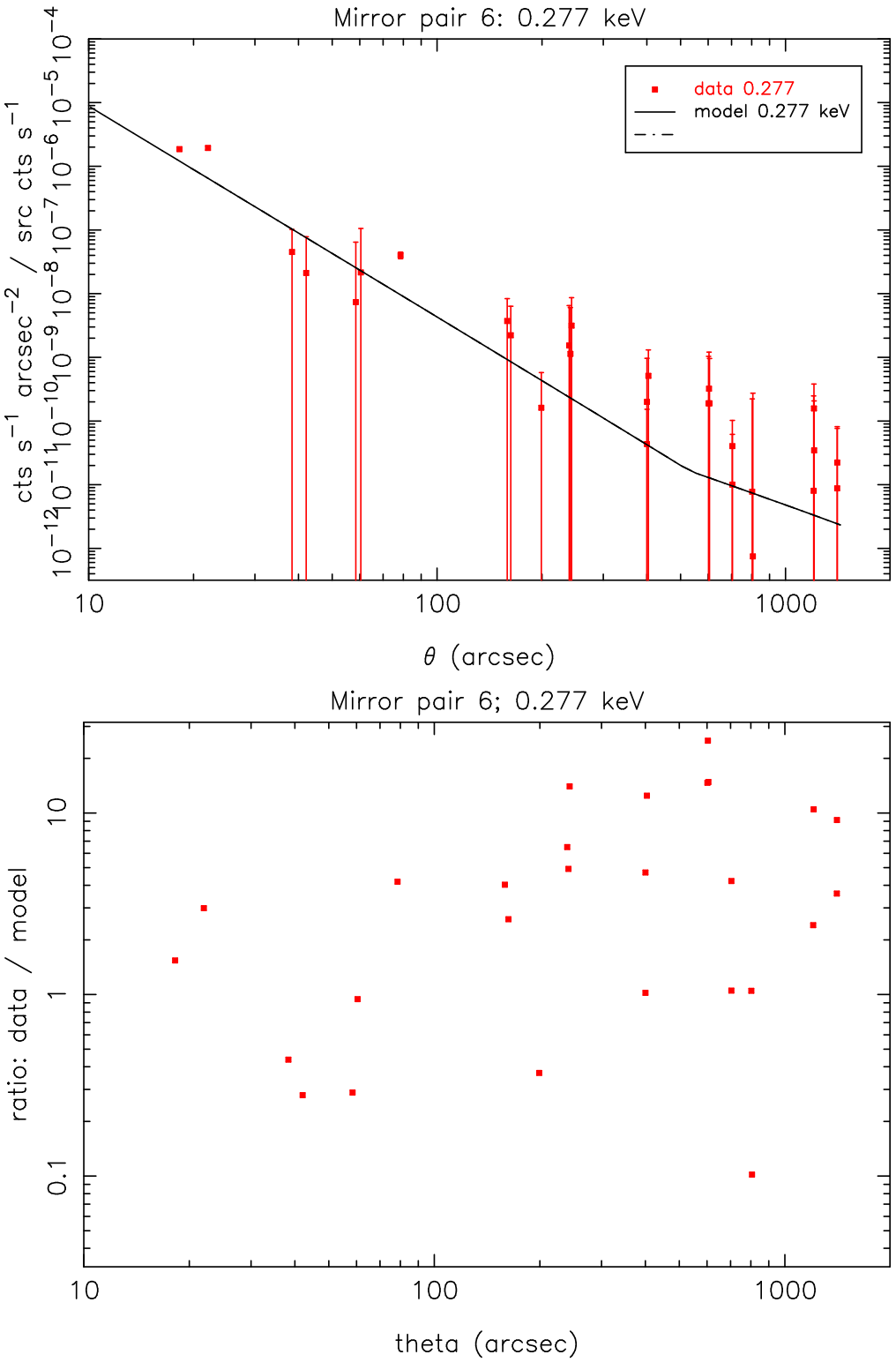

Figure 9: Top: Data *vs.* Model; shell 6, 0.277 keV. Bottom: Data/Model.

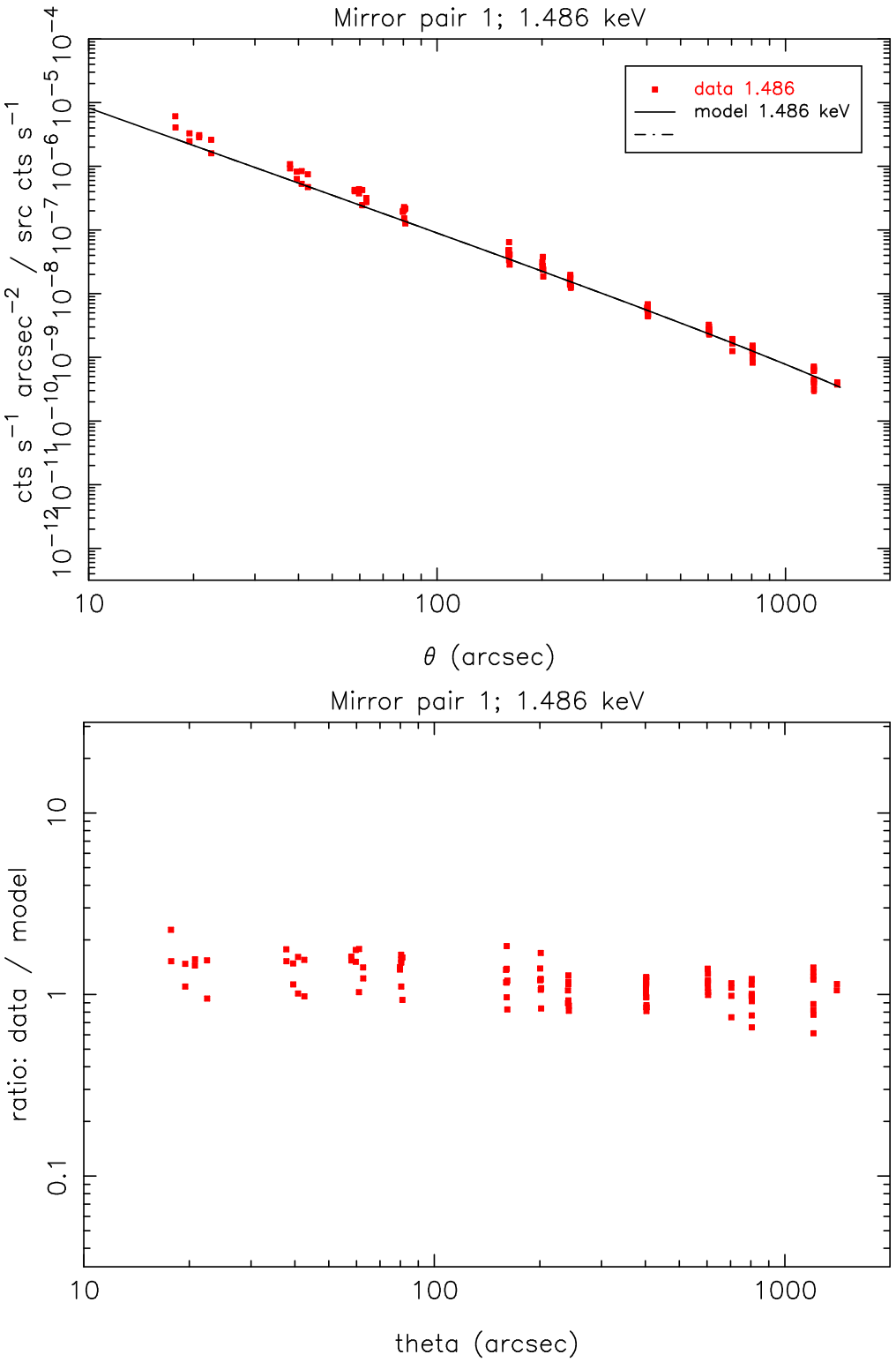

Figure 10: Top: Data *vs.* Model; shell 1, 1.486 keV. Bottom: Data/Model.

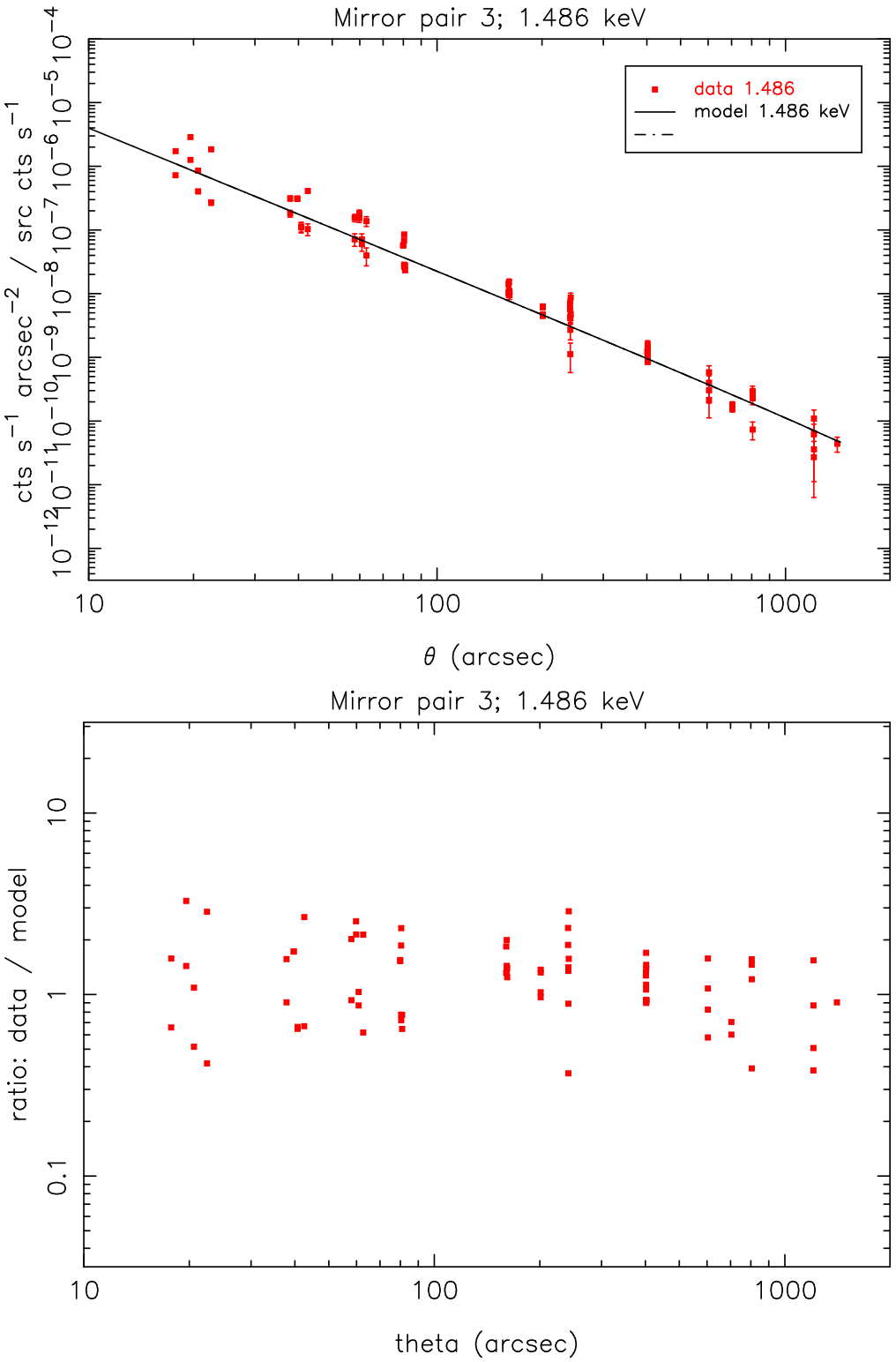

Figure 11: Top: Data *vs.* Model; shell 3, 1.486 keV. Bottom: Data/Model.

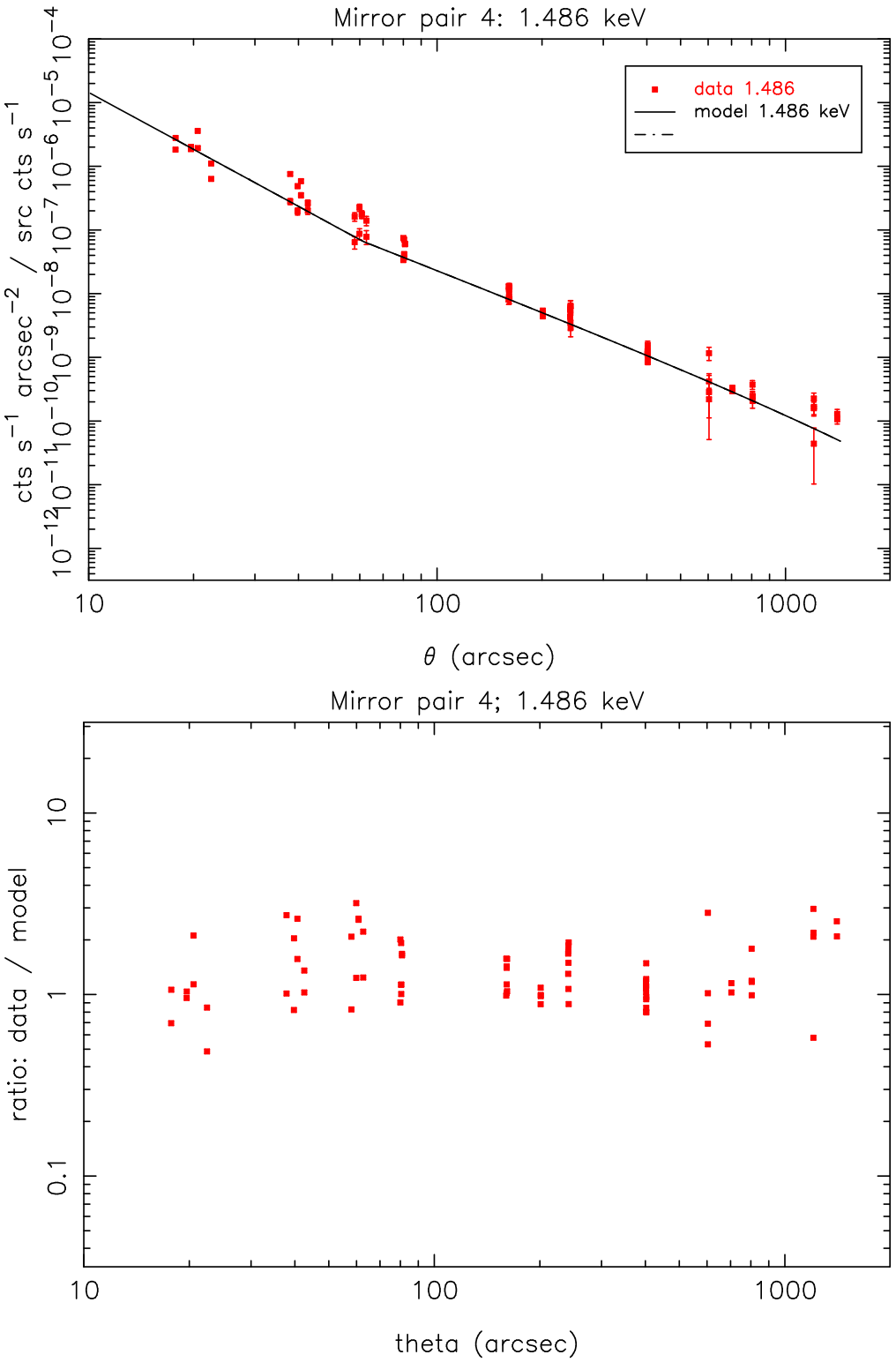

Figure 12: Top: Data *vs.* Model; shell 4, 1.486 keV. Bottom: Data/Model.

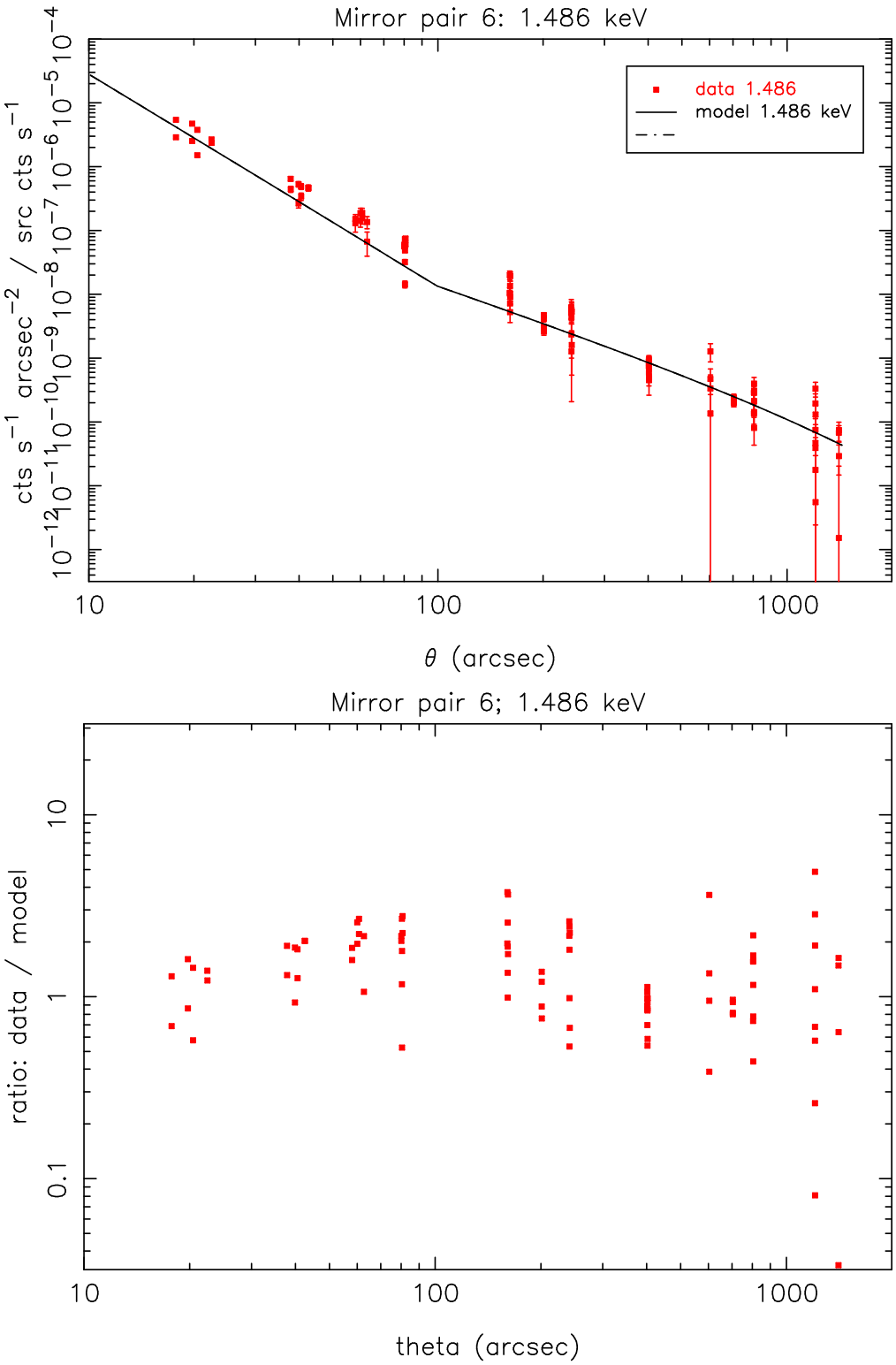

Figure 13: Top: Data *vs.* Model; shell 6, 1.486 keV. Bottom: Data/Model.

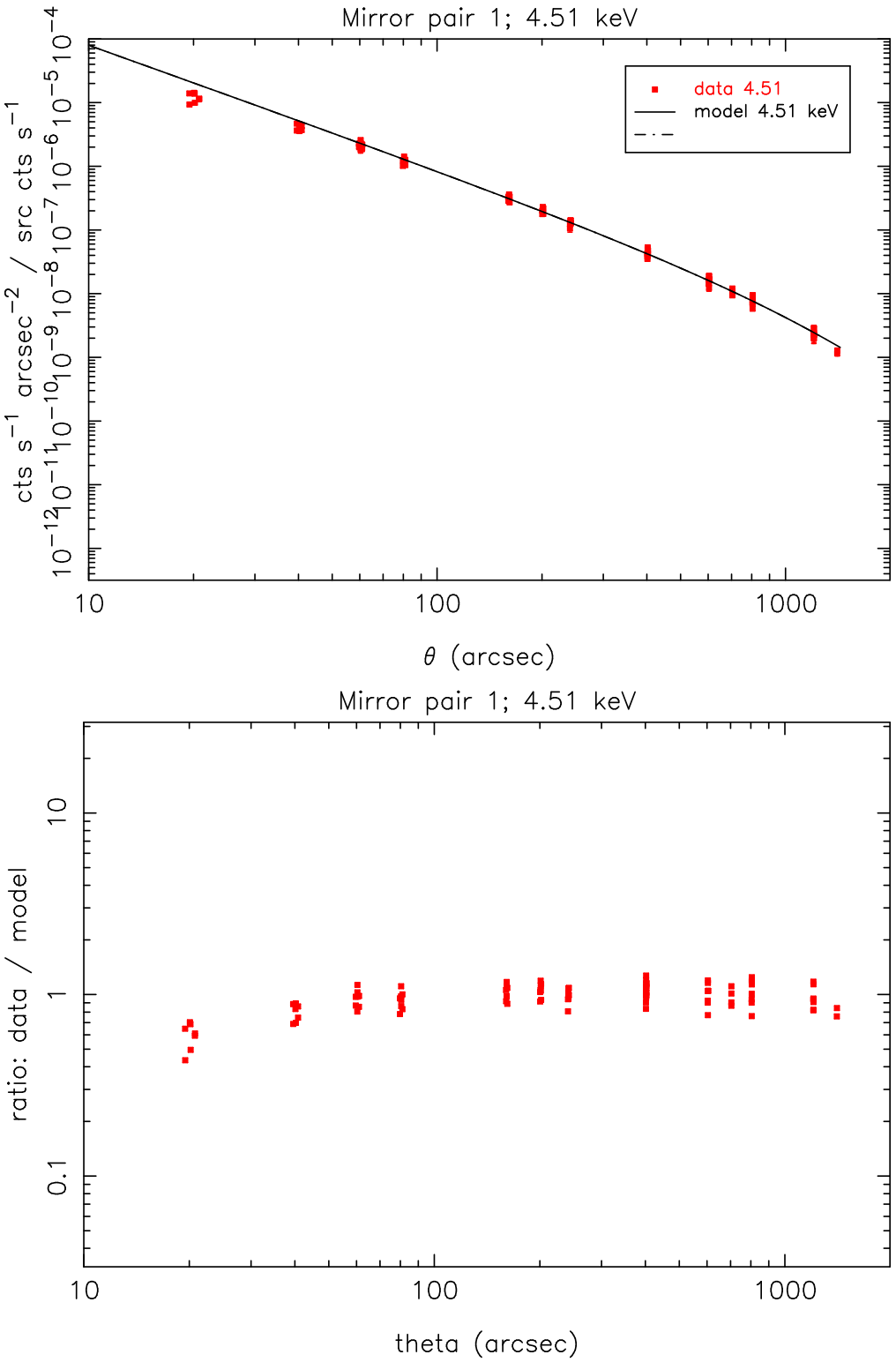

Figure 14: Top: Data *vs.* Model; shell 1, 4.51 keV. Bottom: Data/Model.

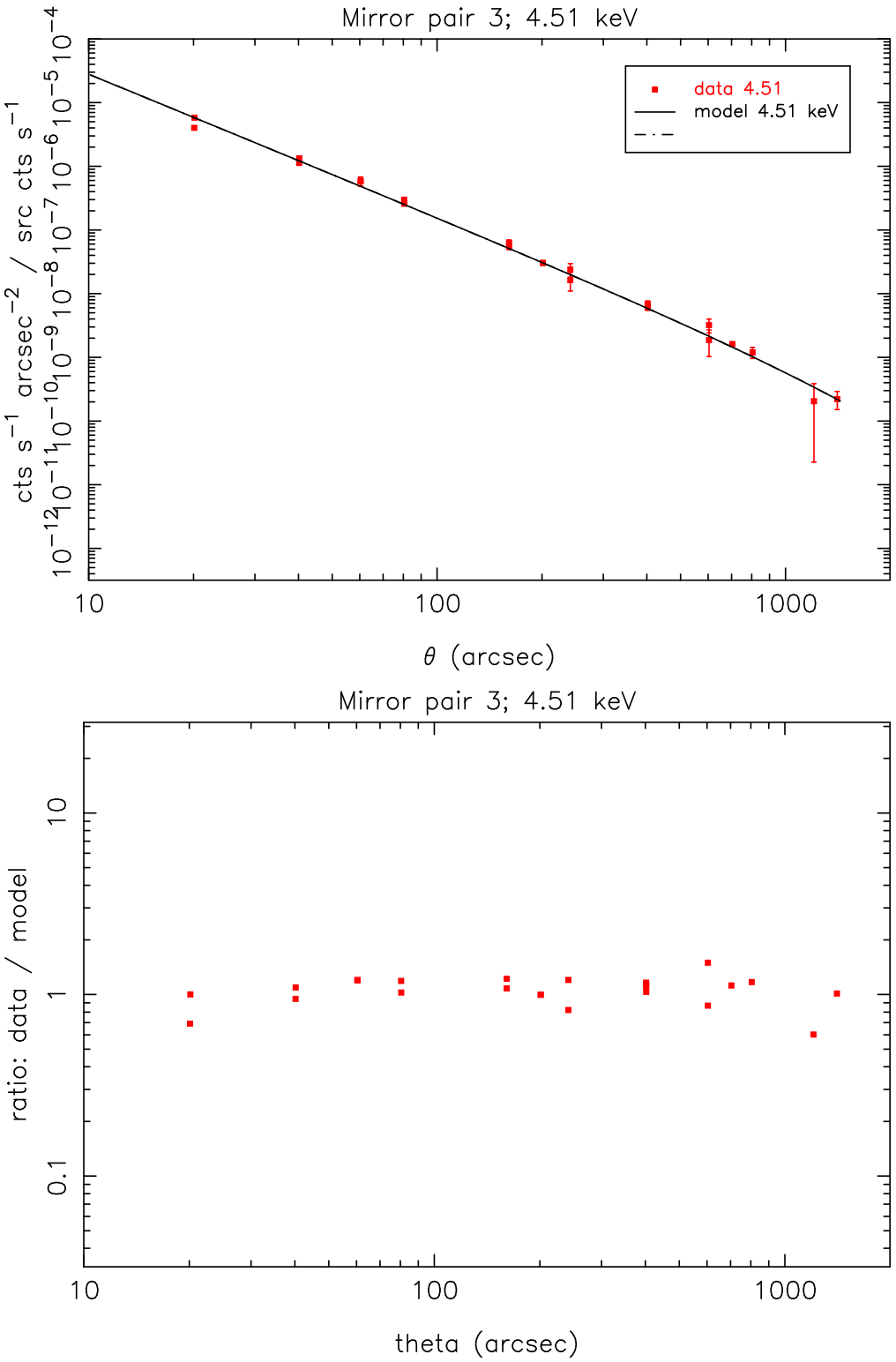

Figure 15: Top: Data *vs.* Model; shell 3, 4.51 keV. Bottom: Data/Model.

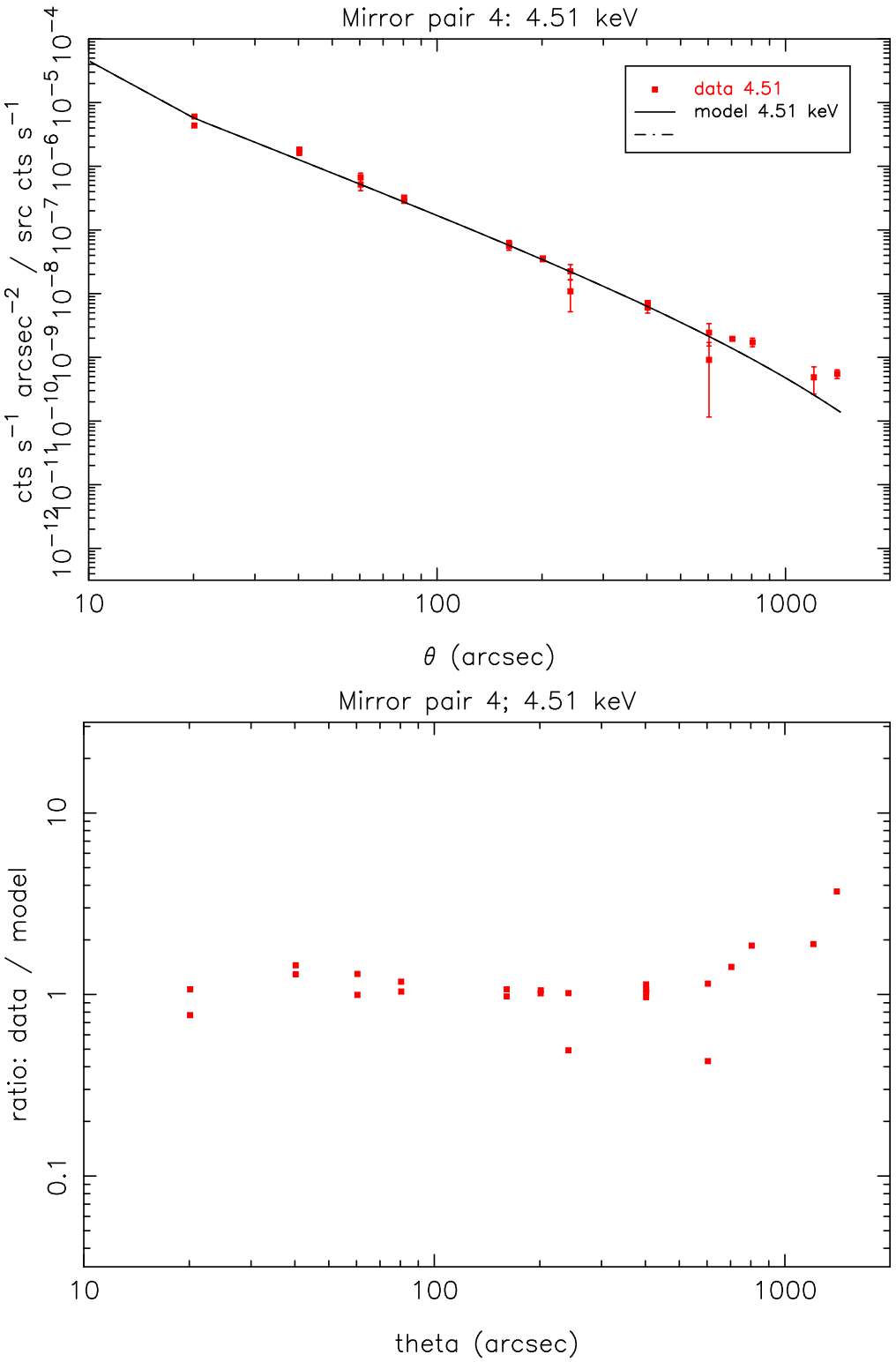

Figure 16: Top: Data *vs.* Model; shell 4, 4.51 keV. Bottom: Data/Model.

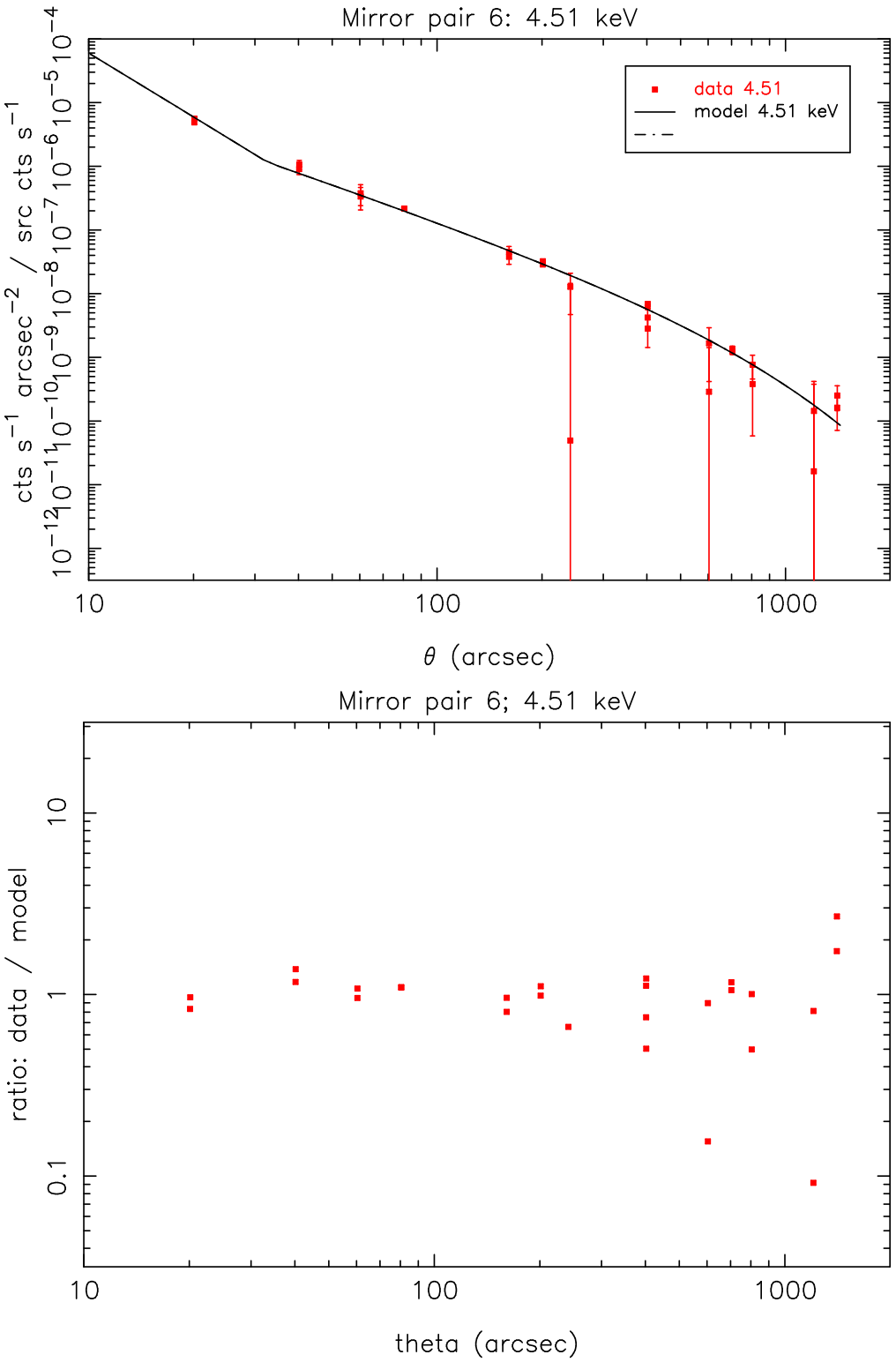

Figure 17: Top: Data *vs.* Model; shell 6, 4.51 keV. Bottom: Data/Model.

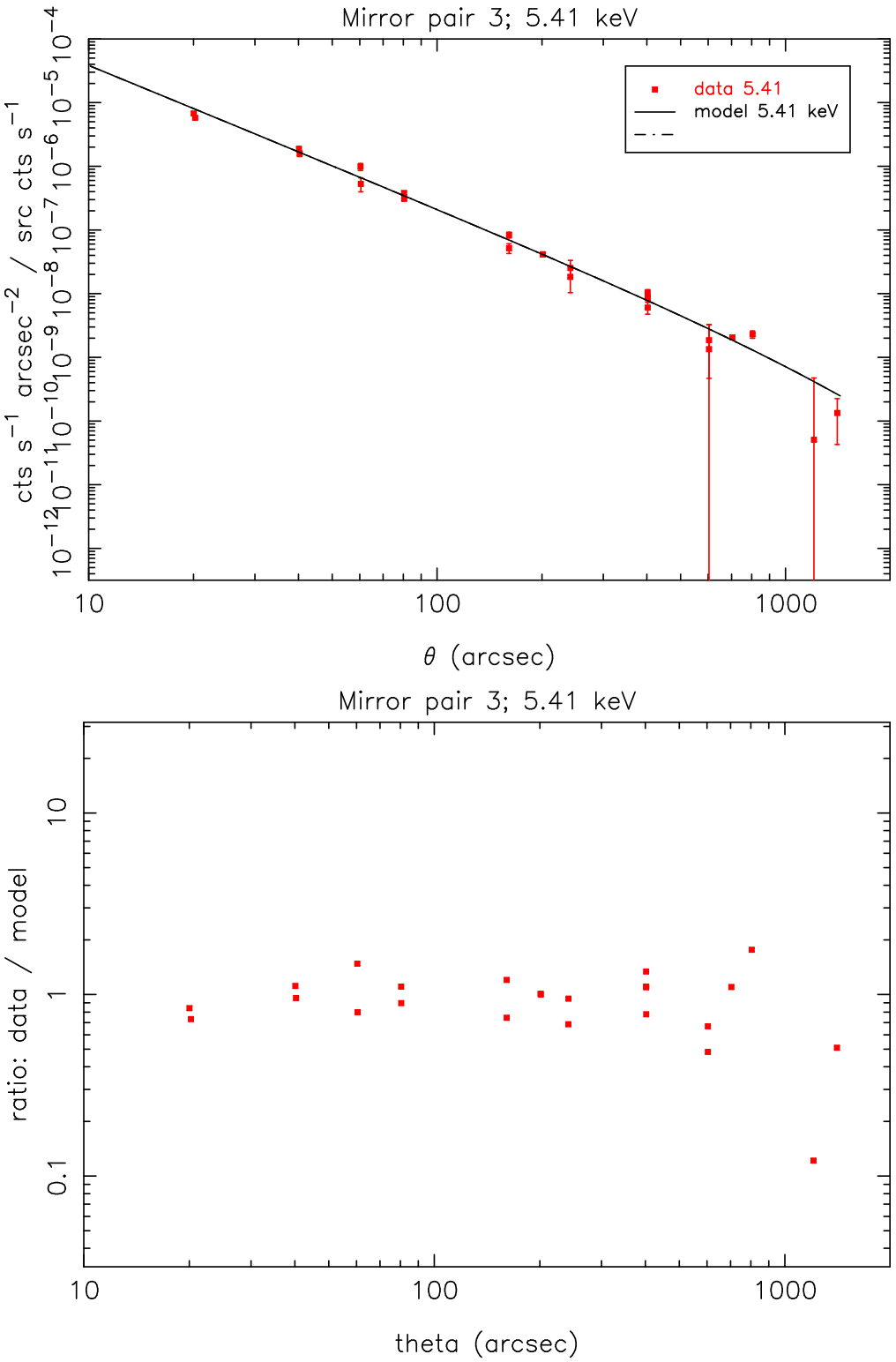

Figure 18: Top: Data *vs.* Model; shell 3, 5.41 keV. Bottom: Data/Model.

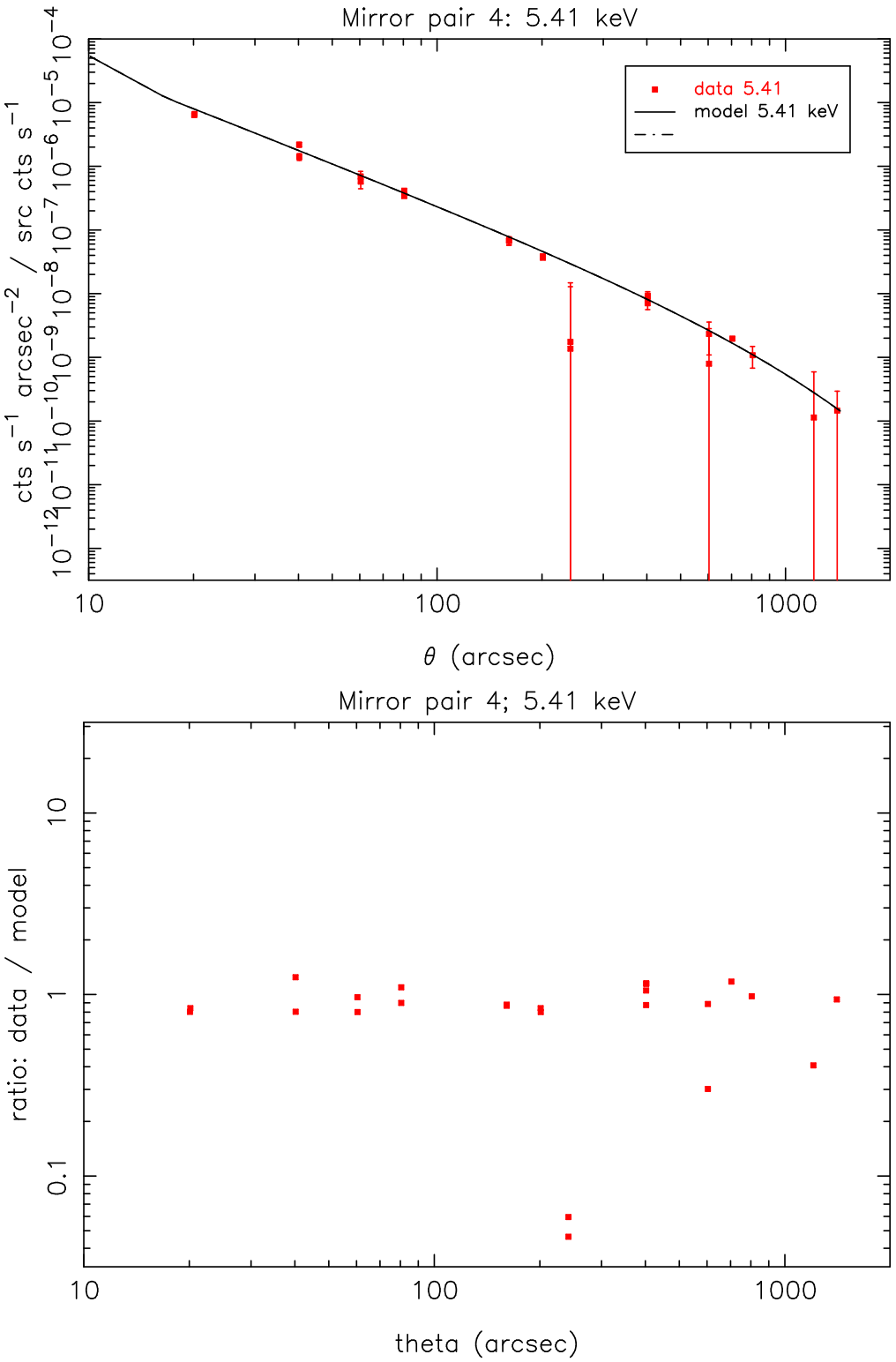

Figure 19: Top: Data *vs.* Model; shell 4, 5.41 keV. Bottom: Data/Model.

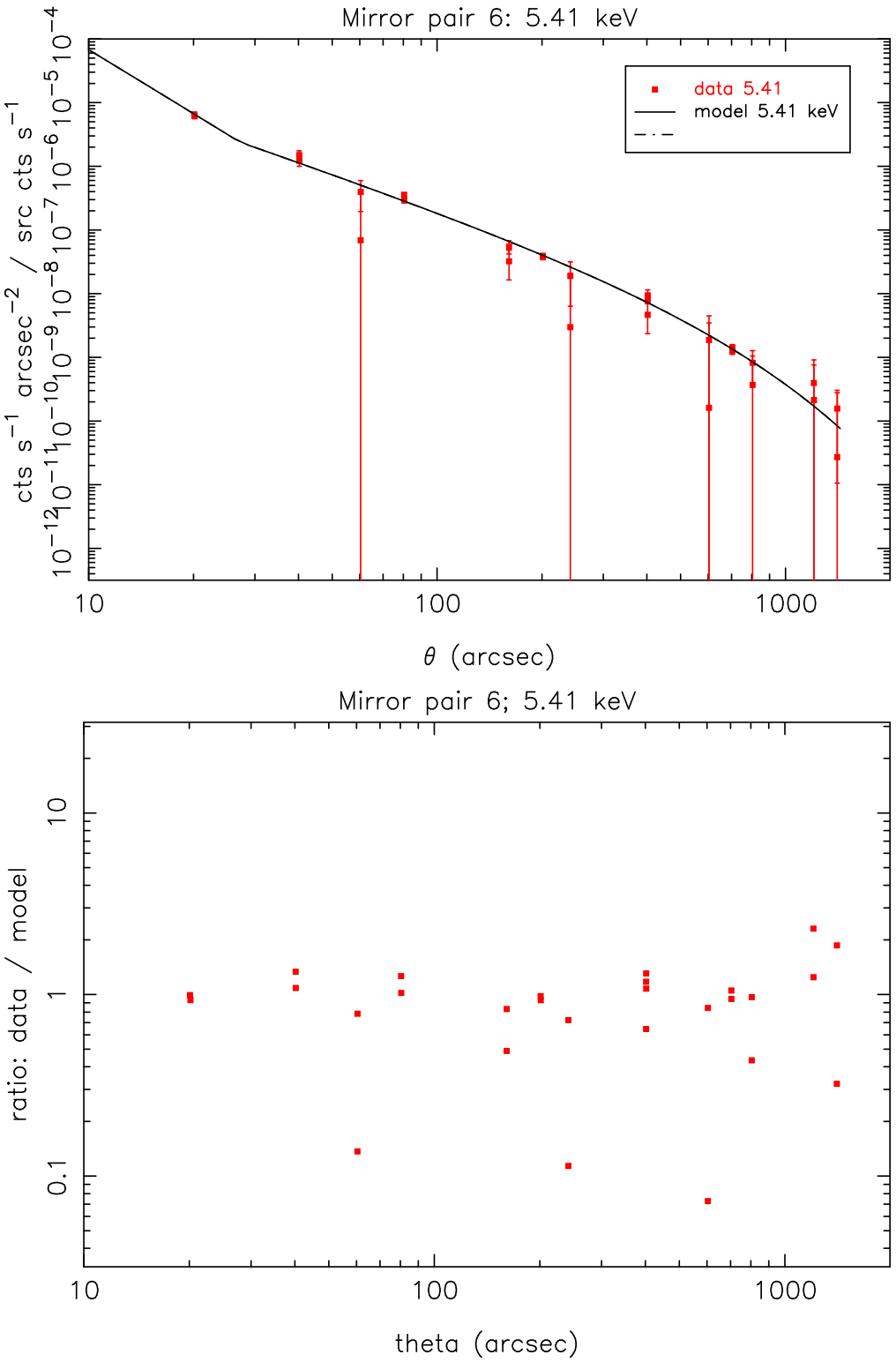

Figure 20: Top: Data *vs.* Model; shell 6, 5.41 keV. Bottom: Data/Model.

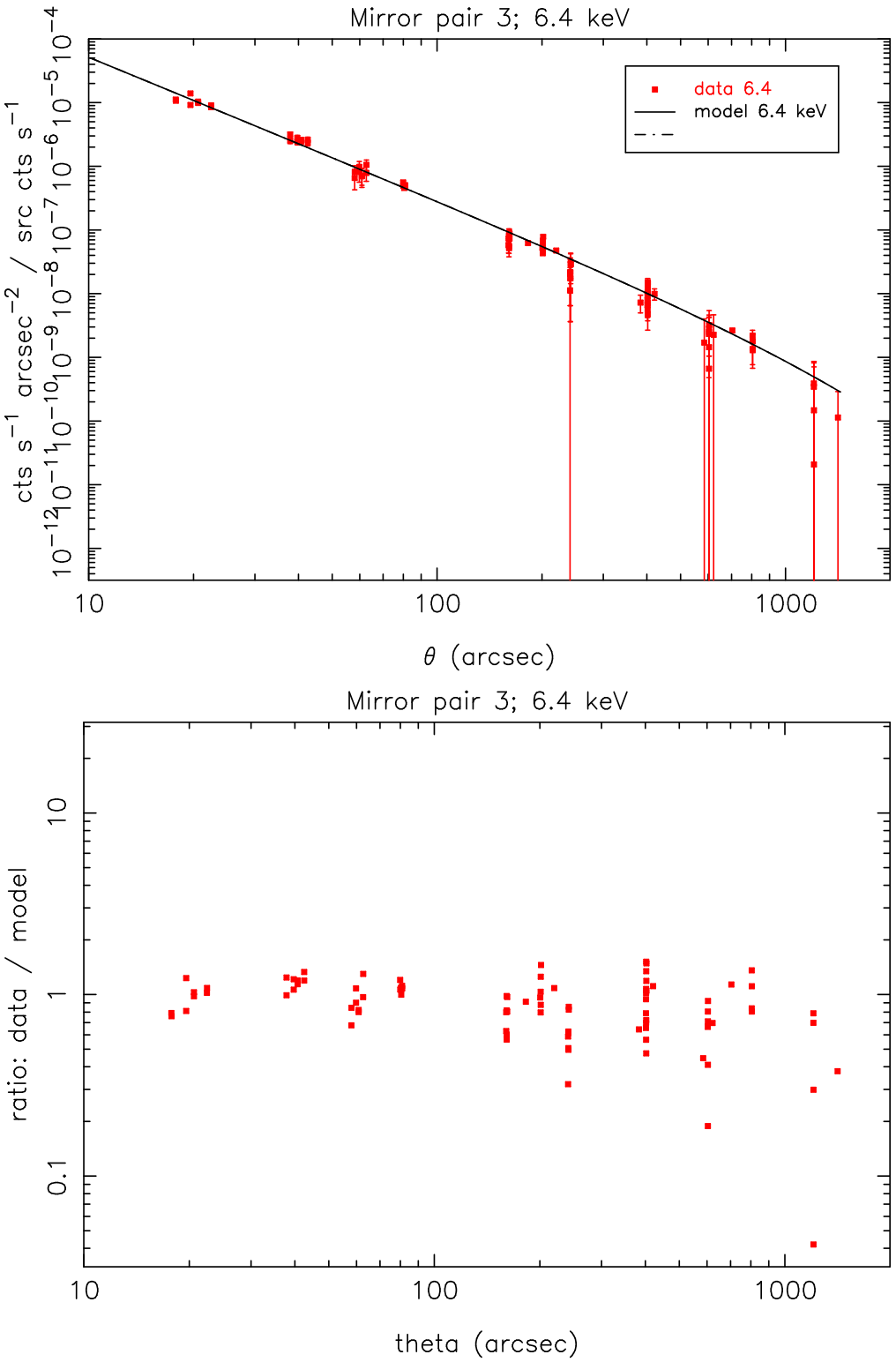

Figure 21: Top: Data *vs.* Model; shell 3, 6.4 keV. Bottom: Data/Model.

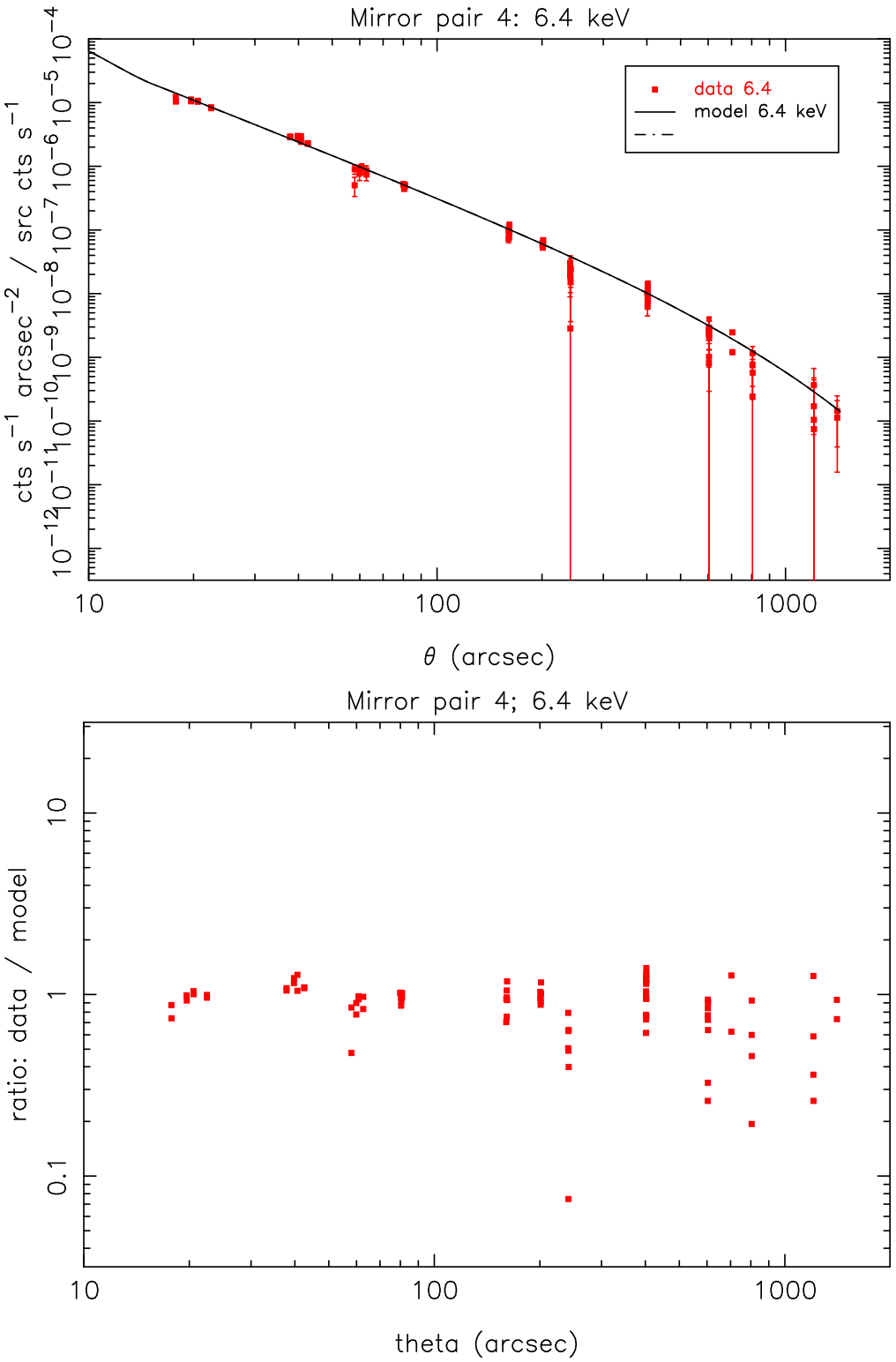

Figure 22: Top: Data *vs.* Model; shell 4, 6.4 keV. Bottom: Data/Model.

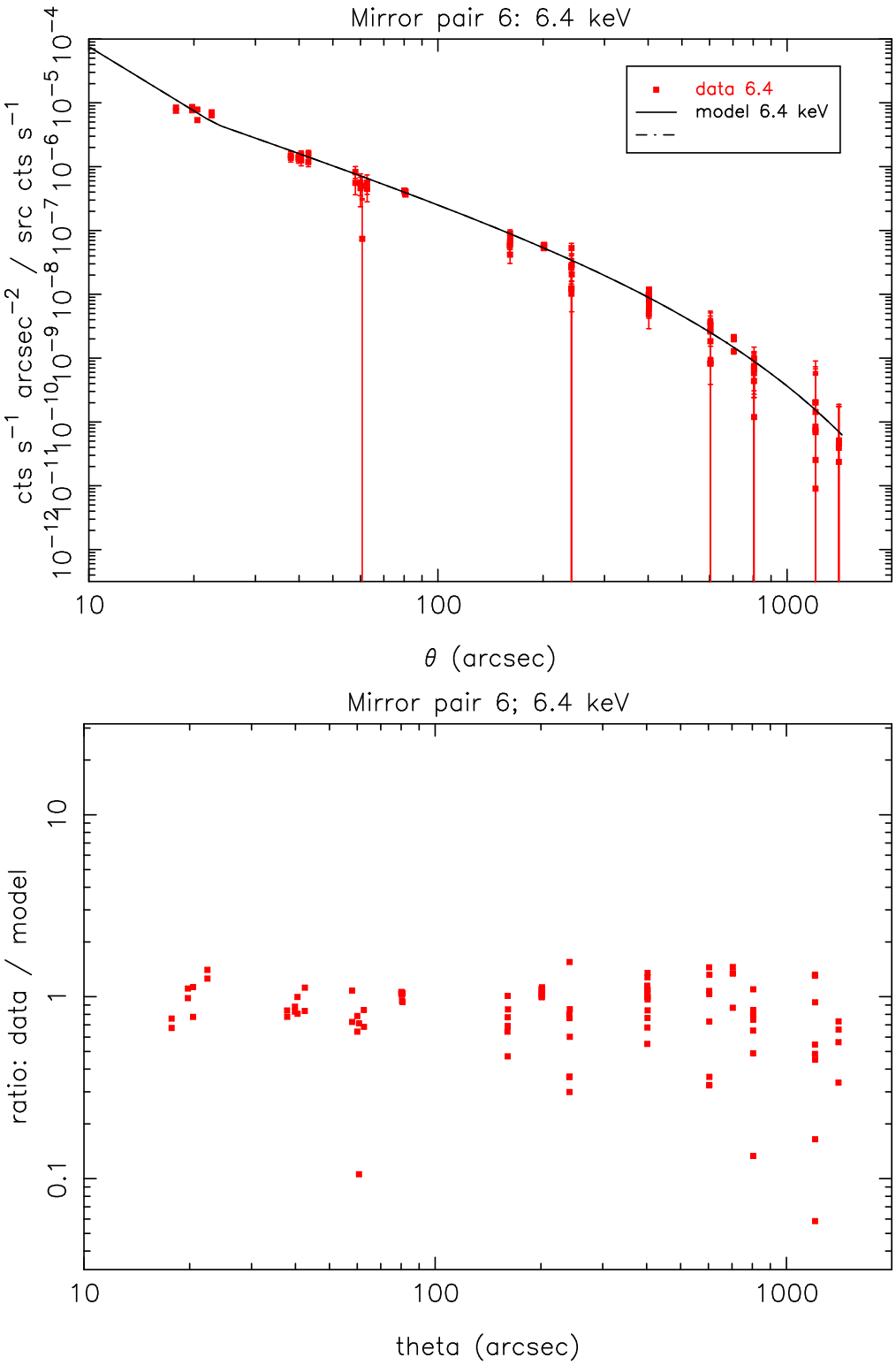

Figure 23: Top: Data *vs.* Model; shell 6, 6.4 keV. Bottom: Data/Model.

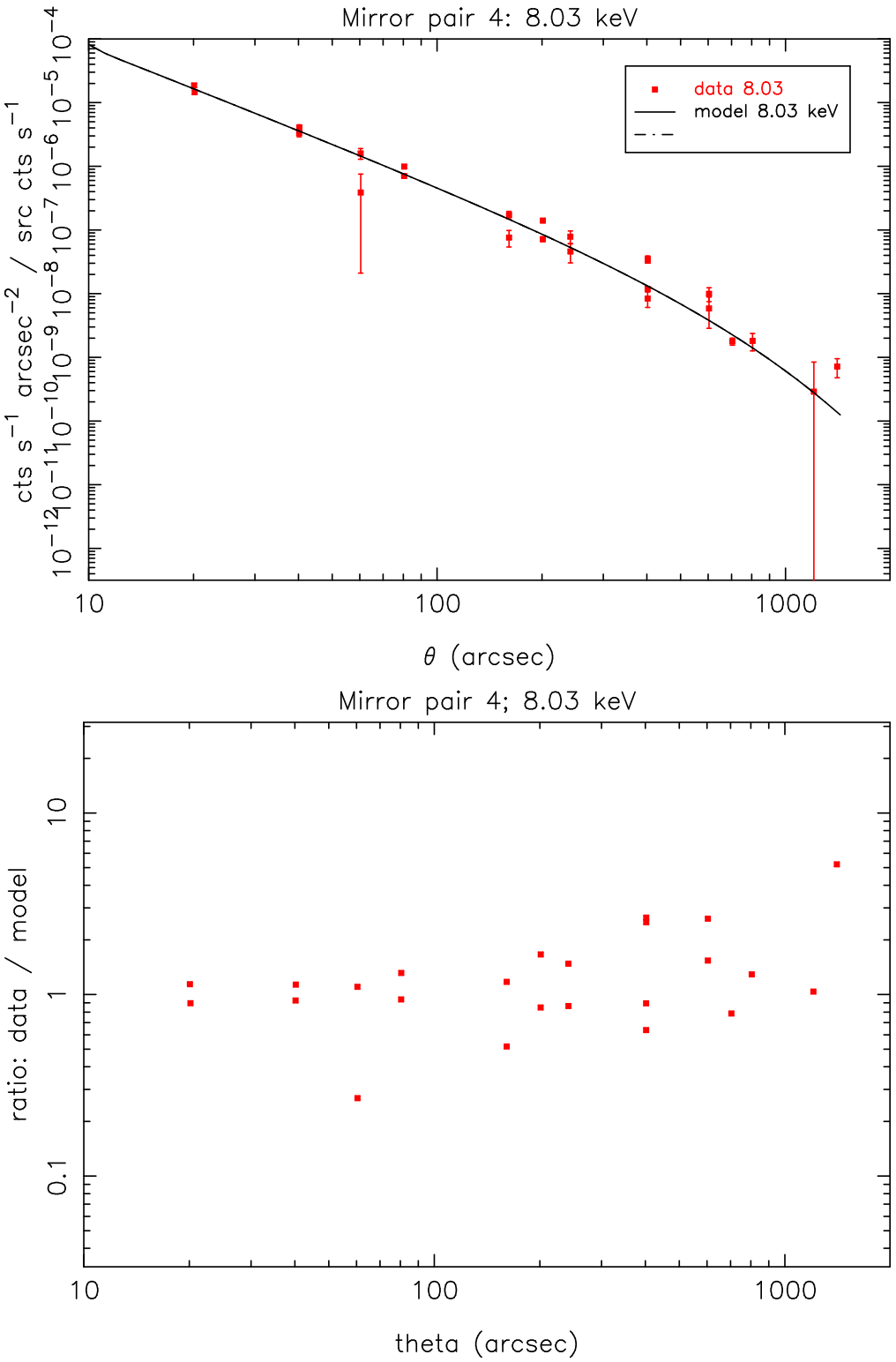

Figure 24: Top: Data *vs.* Model; shell 4, 8.03 keV. Bottom: Data/Model.

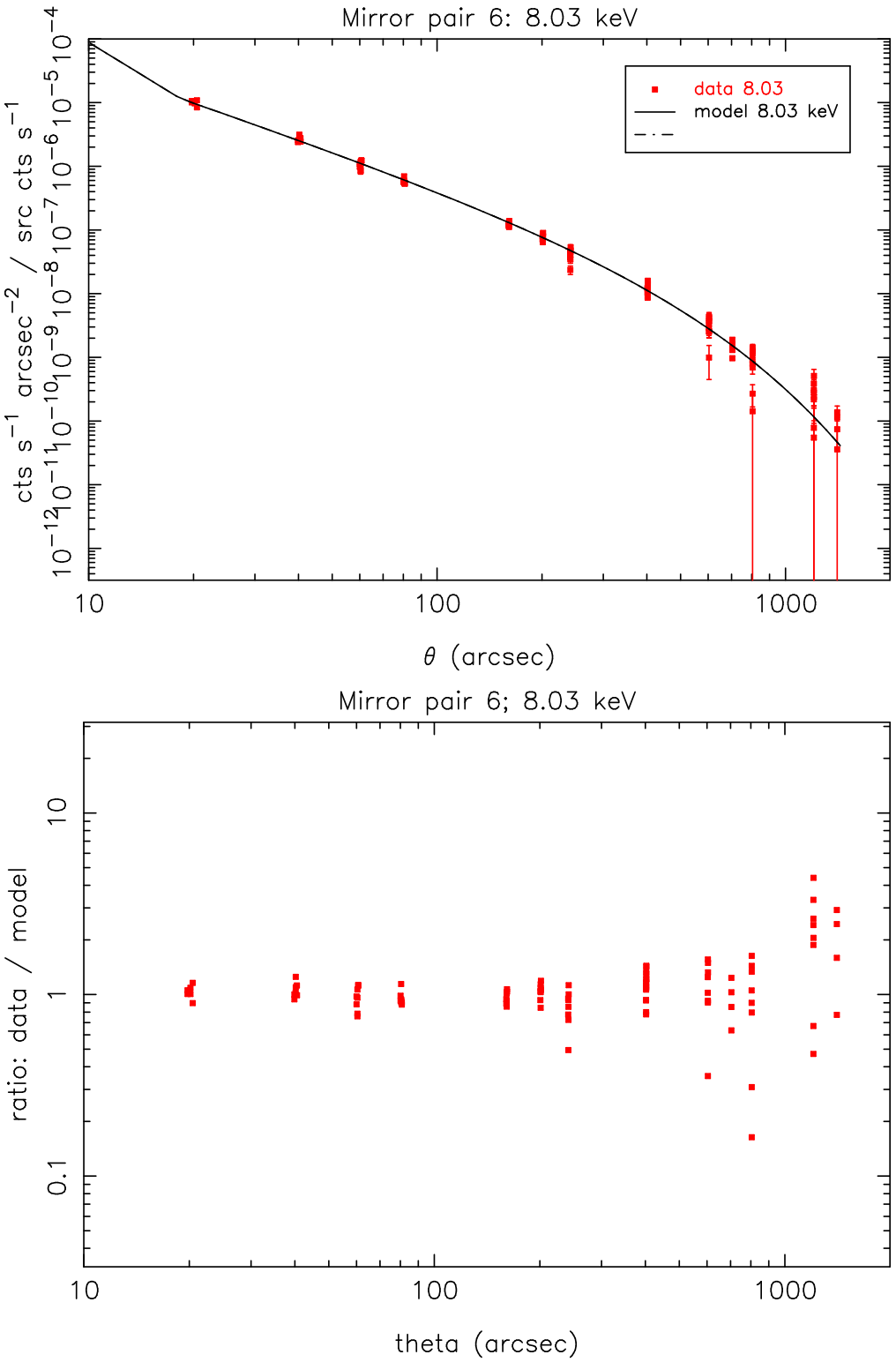

Figure 25: Top: Data *vs.* Model; shell 6, 8.03 keV. Bottom: Data/Model.

E Quadrant Shutter Vignetting

The vignetting limit is estimated as

$$\delta R_{in} = R_{hc} - \left[\frac{R_{hc} - R_{so}}{D_{qs}}\right] D_{fp} \tag{28}$$

and

$$\delta R_{out} = R_{hc} - \left[\frac{R_{hc} - R_{si}}{D_{qs}}\right] D_{fp} \tag{29}$$

where the various radii and distances are indicated in Figs. 26–29. The pinhole is rejected if its center lies within a pinhole radius of δR_{in} or δR_{out} of the specular image; the signs for the offsets are set appropriately depending on which mirror quadrant is under consideration.

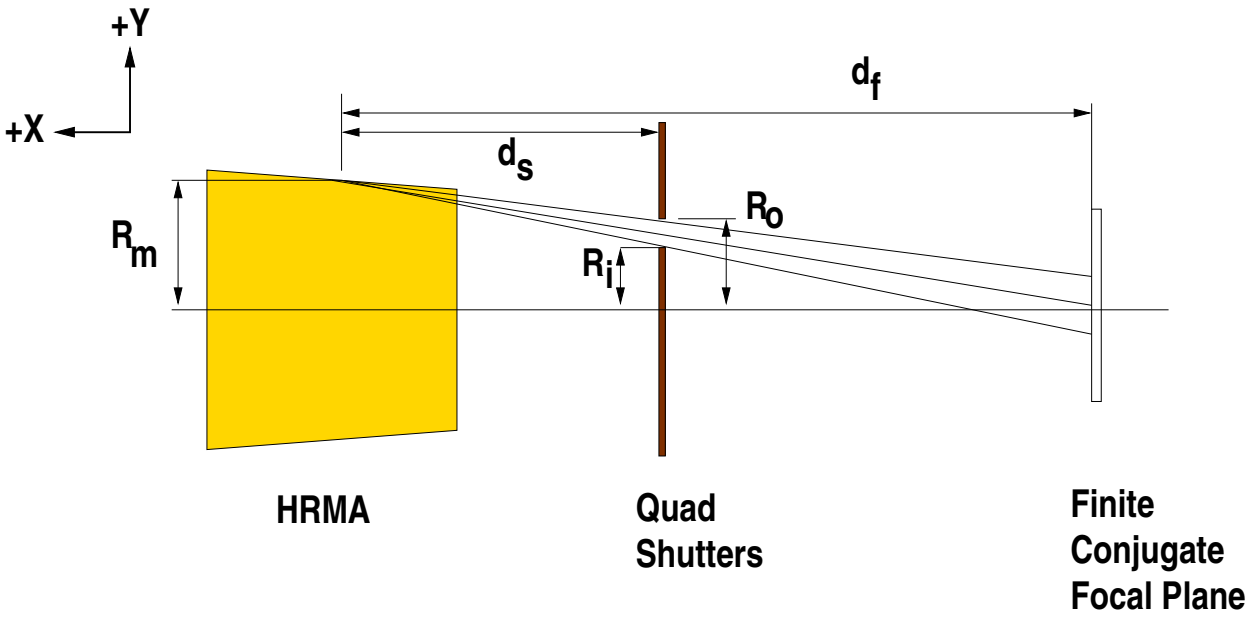

Figure 26: Schematic of the quadrant shutter vignetting.
Schematic of the quadrant shutter vignetting: PS

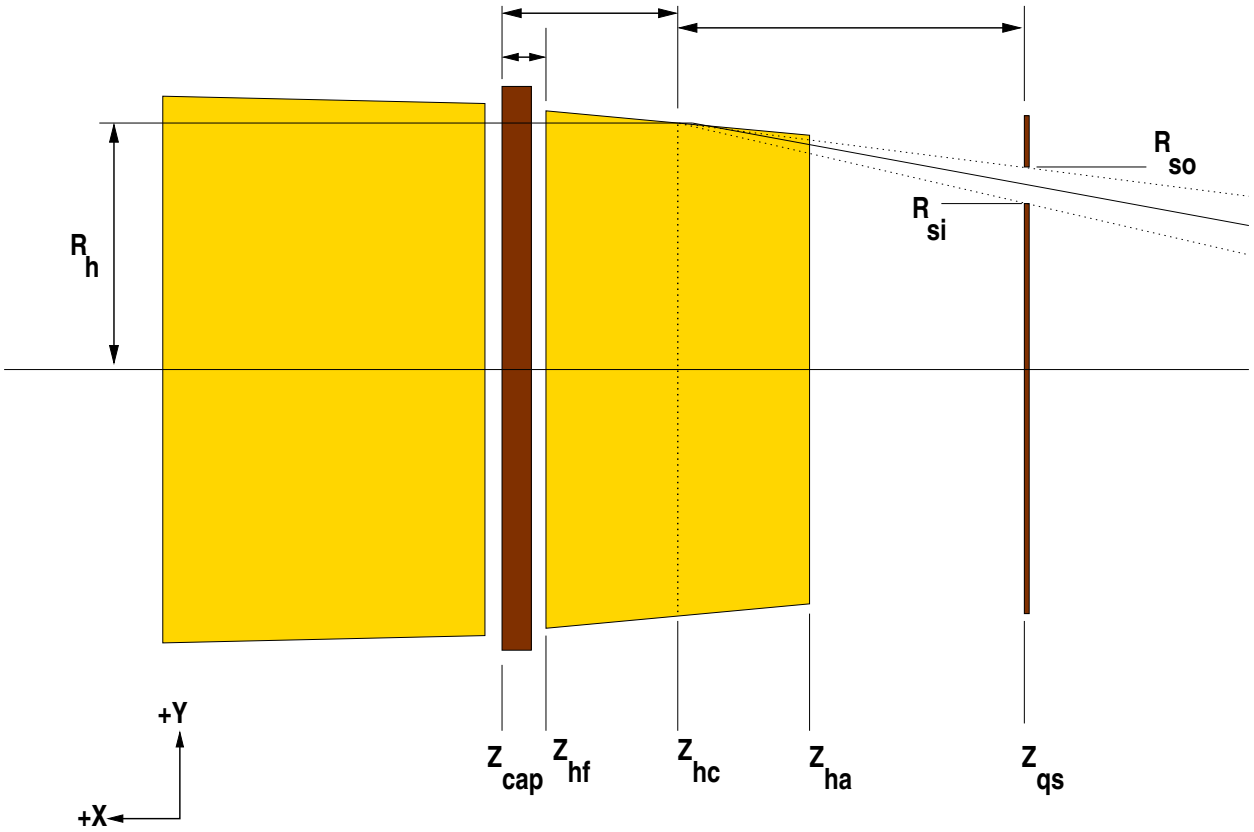

Figure 27: Schematic: closeup of the quadrant shutter vignetting geometry. Z_{hc} is the axial position halfway along the H optic. The heavy line connects the surface point at that axial station to the image position at the finite-conjugate focal plane.
Schematic: closeup of the quadrant shutter vignetting geometry: PS

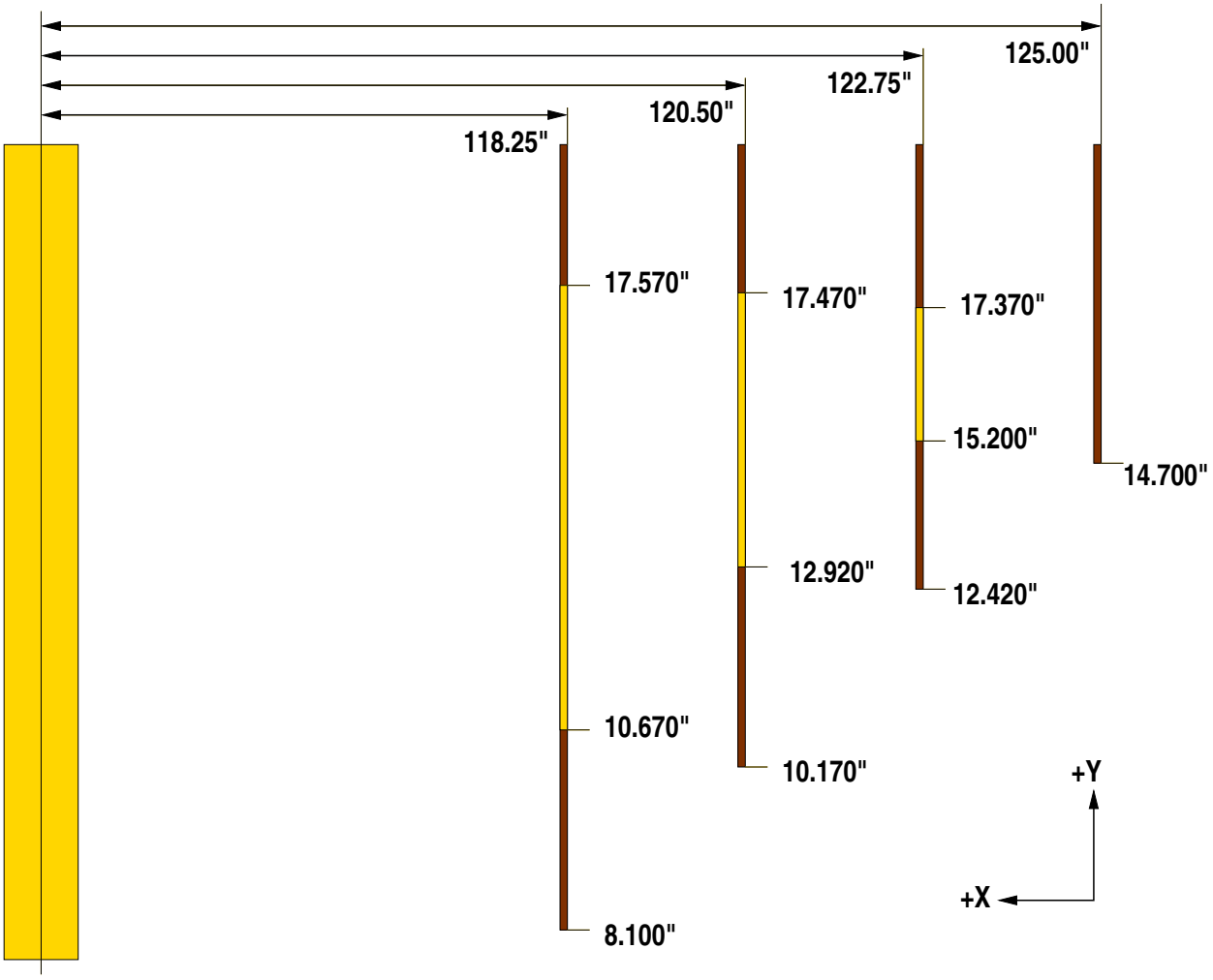

NOTES:
. Axial distances are from the CAP midplane to the –X side of the Y–axis shutters;
The Z–axis shutters are in 0.375" in the +X direction from the Y–axis shutters.
. Tolerance between blades and CAP midplane is of order +/–0.25".

Figure 28: Schematic of the quadrant shutter aperture radii and axial positioning.
Schematic: quadrant shutter radii and axial positioning: PS

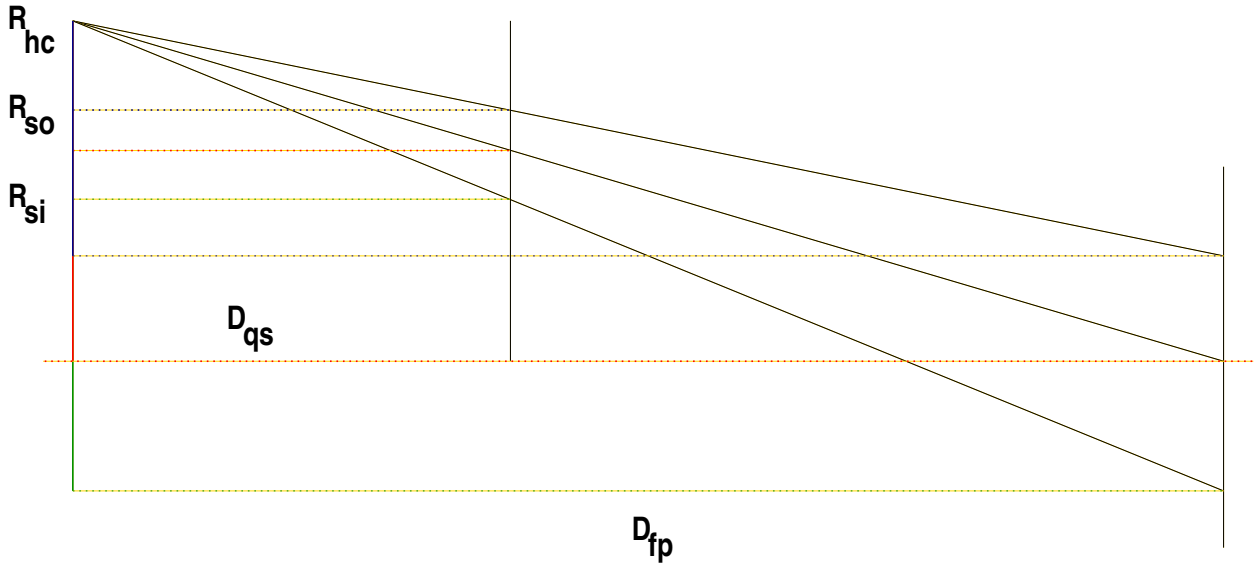

Figure 29: Schematic of the quadrant shutter vignetting calculation.
Schematic: quadrant shutter vignetting calculation: PS